The Astrophysical Journal, 980:53 (19pp), 2025 February 10 https://doi.org/10.3847/1538-4357/ada899
© 2025. The Author(s). Published by the American Astronomical Society.
OPEN ACCESS

Black Hole Supernovae, Their Equation of State Dependence, and Ejecta Composition

Oliver Eggenberger Andersen[1], Evan O'Connor[1], Haakon Andresen[1], André da Silva Schneider[2], and Sean M. Couch[3,4,5]
[1] The Oskar Klein Centre, Department of Astronomy, Stockholm University, AlbaNova, SE-106 91 Stockholm, Sweden; oliver.e.andersen@astro.su.se
[2] Departamento de Física, Universidade Federal de Santa Catarina, Florianópolis, SC 88040-900, Brazil
[3] Department of Physics and Astronomy, Michigan State University, East Lansing, MI 48824, USA
[4] Department of Computational Mathematics, Science, and Engineering, Michigan State University, East Lansing, MI 48824, USA
[5] Facility for Rare Isotope Beams, Michigan State University, East Lansing, MI 48824, USA
Received 2024 November 19; revised 2025 January 2; accepted 2025 January 8; published 2025 February 4

Abstract

Recent literature on core-collapse supernovae suggests that a black hole (BH) can form within ∼1 s of shock revival, while still culminating in a successful supernova. We refer to these as BH supernovae, as they are distinct from other BH formation channels in both timescale and impact on the explosion. We simulate these events self-consistently from core collapse until 20–50 days after collapse using three axisymmetric models of a 60 $M_\odot$ zero-age main-sequence progenitor star and investigate how the composition of the ejecta is impacted by the BH formation. We employ Skyrme-type equations of state (EOSs) and vary the uncertain nucleonic effective mass, which affects the pressure inside the proto–neutron star through the thermal part of the EOS. This results in different BH formation times and explosion energies at BH formation, yielding final explosion energies between 0.06 and 0.72×10^{51} erg with 21.8–23.3 $M_\odot$ of ejecta, of which 0–0.018 $M_\odot$ is ^{56}Ni. Compared to expectations from 1D simulations, we find more nuanced EOS dependences of the explosion dynamics, the mass of the BH remnant, and the elemental composition of the ejecta. We investigate why the explosions survive despite the massive overburden and link the shape of the diagnostic energy curve and character of the ejecta evolution to the progenitor structure.

Unified Astronomy Thesaurus concepts: Core-collapse supernovae (304); Supernovae (1668); Black holes (162); Hydrodynamical simulations (767); Radiative transfer simulations (1967); Neutron stars (1108); General relativity (641); Explosive nucleosynthesis (503); Shocks (2086); Supernova neutrinos (1666); Gravitational instability (668); Supernova dynamics (1664)

Materials only available in the online version of record: animation

1. Introduction

Core-collapse supernovae (CCSNe) play an important role in the Universe. The SN ejecta carries the yields of nucleosynthesis processes occurring throughout the star's life, including at the end, that contribute to the enrichment of the Universe. Furthermore, neutron stars (NSs) and stellar-mass black holes (BHs) are born in CCSNe. Data analysis from X-ray binary observations (F. Özel & P. Freire 2016; J. M. Lattimer 2021) and gravitational-wave interferometers are beginning to map out the population of NSs and BHs (R. Abbott et al. 2023a). The mass distributions of NSs and BHs will be increasingly resolved with more observations and with future detectors (Y. Shao 2022; R. Abbott et al. 2023b). To predict and understand the shape of these distributions, it is crucial that we take into account and understand all NS and BH formation channels. In the conventional theory of CCSNe, the outcome of CC is dichotomous: either the shock wave unbinds the envelope of the star and a NS is left behind, or the stalled shock is not revived and continued accretion onto the proto-NS (PNS) results in BH formation, called failed SNe (E. O'Connor & C. D. Ott 2011a). Failed SNe are often associated with either dim or no electromagnetic signals (R. A. Byrne & M. Fraser 2022), and several studies have searched for and found "disappearing stars" (C. S. Kochanek et al. 2008; T. M. Reynolds et al. 2015; S. M. Adams et al. 2017; C. M. Basinger et al. 2021; J. M. M. Neustadt et al. 2021; K. De et al. 2024). However, there is still no conclusive evidence connecting these candidates to failed SNe (R. A. Byrne & M. Fraser 2022).

Recent advancements in the field, however, have revealed a highly diverse landscape of CCSN outcomes. BHs can form via several paths, all of which need to be accounted for in compact object population synthesis calculations (M. Mapelli 2021; K. Belczynski et al. 2022). In events where the shock is not revived, the outer layers of the star can be expelled as a hydrodynamical response to the neutrino emission in the early postbounce phase (D. K. Nadezhin 1980; A. L. Piro 2013; E. Lovegrove & S. E. Woosley 2013), which can result in a transient and a BH mass that differs from the progenitor mass (E. Lovegrove & S. E. Woosley 2013; R. Fernández et al. 2018; M. Ivanov & R. Fernández 2021; A. da Silva Schneider & E. OConnor 2022).

BHs can form in various ways when the shock is revived. For instance, thermal pressure can temporarily hold a NS above the maximum mass that the cold equation of state (EOS) can support, leading to its collapse into a BH once it cools (T. W. Baumgarte et al. 1996; E. O'Connor & C. D. Ott 2011b). Alternatively, BH formation can occur when initially outgoing matter falls below the escape velocity (e.g., S. A. Colgate 1971; R. A. Chevalier 1989; C. L. Fryer 1999; W. Zhang et al. 2008; T. Ertl et al. 2020), eventually accreting and pushing the NS above the maximum mass that the EOS can support. These events, known as fallback SNe, occur over tens of seconds to hours after shock revival depending on the

Original content from this work may be used under the terms of the Creative Commons Attribution 4.0 licence. Any further distribution of this work must maintain attribution to the author(s) and the title of the work, journal citation and DOI.

fallback mechanism (T.-W. Wong et al. 2014). In fallback SNe, the long timescales between explosion and BH formation limit the impact on the explosion.

A new BH formation channel that is occurring on much shorter timescales than fallback SNe and significantly affecting explosion dynamics is beginning to be unveiled. In 3D simulations, C. Chan et al. (2018), C. Chan et al. (2020), and A. Burrows et al. (2023) demonstrate the possibility of having a successful explosion, while continued accretion of the progenitor core induces BH formation within 0.55–1.5 s after the shock wave is launched. Despite the quick BH formation, the explosions remain successful and their final explosion energies are comparable to that of a garden-variety SN. Multidimensional dynamics appear crucial in precipitating these BH-forming SNe. They enable the explosion to develop along specific solid angles, while the bulk of accretion occurs from other directions, creating conditions for a nonspherical explosion morphology.

Other studies hint toward the viability of these SNe with rapid BH formation as well, where shock revival precedes BH formation in 2D simulations (K.-C. Pan et al. 2018; N. Rahman et al. 2022; B. Sykes et al. 2023; B. Sykes & B. Müller 2024) and in 3D (T. Kuroda et al. 2018; L. Walk et al. 2020; K.-C. Pan et al. 2021; J. Powell et al. 2021). A high-compactness ($\xi_{2.5} = 0.86$; see Equation (4)) 85 $M_\odot$ progenitor is simulated by J. Powell et al. (2021) in 3D and by B. Sykes et al. (2023) in 2D. In both studies, BH formation occurs hundreds of milliseconds after shock revival. The times of shock revival and the times of BH formation are very similar between the two studies (for the same EOS). As the binding energy of the layers above the shock is higher than the diagnostic explosion energy at BH formation, the final fates of the explosions in J. Powell et al. (2021) and B. Sykes et al. (2023) are uncertain. J. Powell et al. (2021) discuss various outcome scenarios involving possible mass ejection. They show that the BH formation time increases in order with the LS220, SFHo, and SFHx EOSs, and point to the thermal dependence of the EOSs as the underlying cause. N. Rahman et al. (2022) simulate high-compactness progenitors ($\xi_{2.5}$ between 0.77 and 0.89) using the SFHo EOS, and witness BH formation within hundreds of milliseconds after shock revival. Their diagnostic explosion energy drops to zero within a few seconds. Still, a shock or sonic wave moves outward carrying 4–7 $\times 10^{49}$ erg, and they estimate mass losses between 0.07 and 3.5 $M_\odot$. Recently, B. Sykes & B. Müller (2024) conducted 2D simulations of eight compact ($\xi_{2.5} > 0.62$) zero-metallicity progenitors with masses ranging from 60 $M_\odot$ to 95 $M_\odot$ using the LS220 EOS. In their simulations, BH formation occurs between 0.12 s and 2.1 s after shock revival, with all explosions surviving and resulting in final explosion energies between $\sim 0.4 \times 10^{51}$ erg and $\sim 2.5 \times 10^{51}$ erg.

We continue to explore this novel BH formation channel. It is distinct from fallback SNe in that it is direct accretion of the collapsing progenitor that causes BH formation, and not ejected material that reverses and accretes at later times. In fallback SNe, BH formation has a small impact on the overall explosion dynamics, whereas the BH formation channel explored here has a large impact on the explosion properties. To place this BH formation channel in a category of its own, between failed SNe and fallback SNe, we will refer to them as black hole supernovae (BHSNe).

When considering the viability and prevalence of BHSNe, part of the answer lies in understanding which progenitors explode and which do not—a quest with a long history that is still ongoing (C. L. Fryer 1999; E. O'Connor & C. D. Ott 2011a; M. Ugliano et al. 2012; O. Pejcha & T. A. Thompson 2015; A. Perego et al. 2015; K. Nakamura et al. 2015; T. Ertl et al. 2016; T. Sukhbold et al. 2016; B. Müller et al. 2016; S. Curtis et al. 2019; K. Ebinger et al. 2020; S. M. Couch et al. 2020; L. Boccioli et al. 2021, 2023). However, more light is being shed on this question with each state-of-the-art simulation and explodability prediction model, along with insights gained from theoretical work on the imbalance of forces that often results in explosions when the silicon–oxygen interface accretes (M. Gogilashvili et al. 2024; L. Boccioli et al. 2025). Recent state-of-the-art simulations indicate that explosions do not only occur for low-compactness progenitors, but may take place across the entire compactness range, with a lower tendency to explode in the middle of the range (A. Burrows et al. 2019, 2023). High-compactness progenitors are particularly interesting for BHSNe due to their high accretion rates, which may fuel an energetic explosion and simultaneously push the PNS above the maximum mass that the combined thermal and nonthermal parts of the EOS can support.

Several studies have shown that the thermal part of the EOS is a significant uncertainty in the outcome of SNe and their multimessenger signals (A. S. da Silva Schneider et al. 2019; A. da Silva Schneider et al. 2020; H. Yasin et al. 2020; O. Eggenberger Andersen et al. 2021). Specifically, A. S. da Silva Schneider et al. (2019) constructed 97 Skyrme-type (T. H. R. Skyrme 1962) finite-temperature EOSs to systematically explore the impact of the parameters that characterize an EOS by performing a Taylor expansion of the energy functional about the nuclear saturation density. For the progenitor used ($\xi_{2.5} = 0.2785$), A. S. da Silva Schneider et al. (2019) find that the uncertainty range for the effective mass of nucleons ($m^\star$), which determines the thermal dependence of their EOSs, has a dominant impact on CCSNe compared to the nonthermal parameters and their uncertainties. Since the PNS temperature generally increases with compactness, the effective mass and thermal part have an even stronger effect in higher-compactness models, as demonstrated by A. da Silva Schneider et al. (2020) in their exploration of the EOS impact on BH formation in spherically symmetric simulations.

In this study, we use a high-compactness 60 $M_\odot$ progenitor and investigate how the thermal part of the EOS affects the outcome of BHSNe. We self-consistently simulate the collapse and shock revival phase, as well as the evolution after BH formation until days after shock breakout. We demonstrate how the explosion dynamics, mass of the BH remnant, final explosion energy, and composition of the SN ejecta all depend on the thermal part of the EOS.

The remainder of the paper is structured as follows: In Section 2, we detail the methodologies used before and after BH formation, the EOSs employed, the calculations used for nucleosynthesis, and features of the progenitor. In Sections 3.1 and 3.2, we present the results before and after BH formation, respectively. We analyze the evolution of the ejecta composition in Section 3.3. In Section 4, we discuss how the explosions survive through the massive overburden and how our results may transfer to 3D. We summarize and conclude in Section 5.

2. Methods

We utilize the FLASH (v4) simulation framework (B. Fryxell et al. 2000; A. Dubey et al. 2009), modified for

simulating CCSNe (S. M. Couch 2013; S. M. Couch & E. P. O'Connor 2014; E. P. O'Connor & S. M. Couch 2018a, 2018b). We relay the methods in two parts: (1) the collapse phase until BH formation, which captures the evolution until ∼1.5 s postbounce and (2) the post-BH-formation phase, where we mask the BH central region to track the evolution of the explosion without an energy source from the PNS. This phase captures the evolution between at least ∼1.5 s and ∼22 days, illustrating how the shock disrupts the star.

2.1. Evolution Before Black Hole Formation

We evolve the collapse phase in 1D until 20 ms after bounce, from which point we continue the simulations in 2D under the assumption of axisymmetry in cylindrical geometry. The domain extends $\pm 8 \times 10^{11}$ cm along the cylindrical axis and 8×10^{11} cm along the radial axis and is placed onto a grid of 20×10 blocks. Each block has 16×16 zones. Eighteen levels of adaptive mesh refinement are allowed, yielding a finest grid spacing of 281 m. Mesh refinements occur based on density and pressure gradients, and above 90 km we limit the resolution so that an effective resolution of $\sim 0.^{\circ}6$ is maintained. We utilize Newtonian hydrodynamics with an effective general relativistic gravitational potential (Case A in A. Marek et al. 2006). This approach has been demonstrated to effectively capture the general relativistic effects in CCSNe (A. Marek et al. 2006; B. Müller et al. 2012; E. P. O'Connor & S. M. Couch 2018a). There is good agreement in BH formation times in 1D when comparing to an effective potential and a full general relativistic treatment (A. da Silva Schneider et al. 2020). We propagate the time evolution using a second-order Runge–Kutta method (S. M. Couch et al. 2021). Reconstruction is performed with the WENO-Z method (R. Borges et al. 2008) and fluxes between zones are calculated with the HLLC Riemann solver (E. F. Toro et al. 1994). For zones near shocks, the HLLE Riemann solver (B. Einfeldt 1987) is used. For neutrino transport we evolve the first two moments of the neutrino distribution function with an analytic M1 closure (M. Shibata et al. 2011; E. P. O'Connor & S. M. Couch 2018a). Twelve logarithmically spaced energy groups between 1 MeV and ∼315 MeV are used for three species of neutrinos: electron neutrinos (ν_e), electron antineutrinos ($\bar{\nu}_e$), and the composite group of heavy lepton neutrinos and their antineutrinos (ν_x). Neutrino opacities are calculated using `NuLib` (E. O'Connor 2015) and are the baseline set from E. P. O'Connor & S. M. Couch (2018b), with the inclusion of effective mean field and virial corrections (C. J. Horowitz et al. 2017) as well as inelastic scattering of neutrinos on electrons following S. W. Bruenn (1985).

When performing initial 1D tests with a wide range of time steps and several time-evolution solvers in the neutrino transport, we found that the time of BH formation can shift by up to 100 ms depending on the setup. Decreasing the time step led to faster BH formation across all solvers. In terms of BH formation times, we found that the two-step forward Euler method is more consistent than a standard second-order Runge–Kutta method, which we link to the velocity-dependent treatment of the fluxes in the asymptotic limit. Therefore, we use the two-step forward Euler scheme for the 2D simulations, with a time-step size such that the corresponding 1D simulation forms a BH within 30 ms of the earliest BH formation time we observed across all the 1D simulations. It is unclear whether the effect observed in 1D persists in 2D or is washed out when an extra degree of freedom is included. Nevertheless, our 1D test simulations highlight an important, albeit small, source of uncertainty in numerical simulations.

2.2. Evolution After Black Hole Formation

Similar to the approach of C. Chan et al. (2018), N. Rahman et al. (2022), B. Sykes et al. (2023), and more specifically A. da Silva Schneider & E. OConnor (2022), we excise the central region when the BH forms and continue the evolution until at least ∼22 days. At BH formation we set the radius of this mask to 150 km and increase its size by $100\,\mathrm{km\,s^{-1}}$, imposing a maximum radius of 2×10^6 km. To verify that this mask size and its edge velocity are reasonably large, we run a model for 8 s with a mask radius of 50 km and expansion velocity of 50 km $\mathrm{s^{-1}}$. The explosion energy evolution is nearly indistinguishable from the production run in this paper.

The material inside the mask is collected into a point mass, as is the material that subsequently accretes into the "BH." We create a low-pressure region inside the mask by setting the density, temperature, and internal energy to a small fraction of their values outside the mask. This allows the material to freely flow into the mask and is effectively an outflow boundary condition. We do not evolve the neutrino radiation after BH formation because, to a good approximation, there is no longer a source for neutrinos. Since `FLASH` is fundamentally a Newtonian hydrodynamics code, we estimate the gravitational mass ($M_{\rm grav}$) of the compact object at time t by subtracting the mass-energy radiated away by neutrinos from the baryonic mass ($M_{\rm bary}$):

$$M_{\rm grav} = M_{\rm bary} - \frac{1}{c^2}\sum_{\nu}\int_0^t L_\nu(t')dt', \tag{1}$$

where L_ν is the neutrino luminosity from species ν. We get the point mass at the time of BH formation ($t_{\rm BH}$) by inserting $t = t_{\rm BH}$ into Equation (1).

When applying the excision mask at BH formation for each simulation, we also extend the domain by creating a larger grid filled with the progenitor data, then map the simulated 2D data onto this grid. At this time we extend the grid from 8×10^{11} cm to 1.024×10^{14} cm. We perform one more such mapping at ∼700 s, extending the domain out to 8.192×10^{14} cm. We add a low-density, artificial 2.1 $M_\odot$ atmosphere outside the surface of the star at 1.79×10^{14} cm. We set the temperature (T) and electron fraction (Y_e) in the atmosphere to the surface values and assign a density (ρ) of 1.2×10^{-12} g $\mathrm{cm^{-3}}$ (close to the minimum of the EOS). We arbitrarily designate the material in the atmosphere as neutrons to avoid interference with other species when tracking the composition of the ejecta. With this atmosphere in place we follow the evolution until days after the shock breakout. At the time of the second mapping, at ∼700 s, we change the reconstruction method from the spatially fifth-order accurate WENO-Z to a second-order accurate total variation diminishing(TVD) scheme (A. Harten 1983) due to issues encountered at the sharp density interfaces in the "Rayleigh–Taylor" bullets occurring behind the reverse shock (see, e.g., K. Kifonidis et al. 2003; M. A. Sandoval et al. 2021). Although many such bullets are created in our simulations at late times, fewer emerge when using the more diffusive TVD reconstructor compared to when using WENO-Z. Switching to TVD significantly earlier than 700 s leads to a slight difference in the explosion energy. Although there is no significant effect on the total mass accretion evolution, fewer heavy elements

(such as ^{56}Ni) accrete onto the BH. Switching after 700 s does not impact the composition or the explosion energy.

2.3. Equation of State

The hydrodynamic equations are closed using a hybrid EOS (M. Witt et al. 2021). At low densities, we use the Y_e-based Helmholtz EOS (F. X. Timmes & F. D. Swesty 2000), which bridges at a transition density to a Skyrme-type nuclear EOS for higher densities. We refer to A. S. da Silva Schneider et al. (2019), A. da Silva Schneider et al. (2020), and O. Eggenberger Andersen et al. (2021) for details on the nuclear EOSs used and describe the most relevant aspects for this work here.

We deploy the baseline EOS from A. S. da Silva Schneider et al. (2019) in the `m0.75` model, where the effective mass of nucleons for symmetric matter at nuclear saturation density is 0.75, expressed as a fraction of the vacuum mass. Keeping all other parameters in the EOS fixed, we vary the effective mass by 2σ above (model `m0.95`) and below the baseline value (model `m0.55`). The effective masses of neutrons and protons, $m_n^\star$ and $m_p^\star$, primarily determine the temperature-dependent part of the EOS via the kinetic energy per baryon term, $\epsilon_{\rm kin}$:

$$\epsilon_{\rm kin}(n, y, T) = \frac{\sqrt{2}}{\pi^2\hbar^3 n}\frac{T^{5/2}}{}(m_n^{\star 3/2}F_{3/2}(\eta_n) + m_p^{\star 3/2}F_{3/2}(\eta_p)). \quad (2)$$

Here, $F_{3/2}$ is a Fermi integral using the degeneracy parameters η_n and η_p (see A. S. da Silva Schneider et al. 2019), n is the baryon number density, T is the temperature, and y is the proton fraction, which enters into the expression for the effective mass:

$$\frac{\hbar^2}{2m_t^\star} = \frac{\hbar^2}{2m_t} + \alpha_1 n_t + \alpha_2 n_{-t}, \quad (3)$$

where α_i are parameters in the Skyrme model and m_t are the nucleon vacuum masses. If $t = n$ then $-t = p$ and vice versa. This is only one possible parameterization of the effective mass, which depends on the proton and neutron densities. We note that more complex parameterizations exist (C. Constantinou et al. 2015).

2.4. Determining Nucleosynthetic Yields

At the time we transition from the CC evolution to the post-CC evolution we populate the entire simulation domain with a detailed set of compositions that we then advect through the subsequent explosion phase. A. Sieverding et al. (2023) show that an alternative method to using tracer particles is to generate the particle trajectories during postprocessing by integrating the equations of motion, i.e., $d\vec{x}(t)/dt = \vec{v}$, backward (or forward) in time. The backward integration method is ideal for systematically populating a domain at a given time since one can control the location where the yields are to be determined. This is the method we utilize here.

In our case, we use backward integration of the equations of motion to obtain a representative past history of each computational zone. To limit the number of total trajectories, we only have one trajectory for each 2×2 computational zone and we assume the yields are then constant over the four zones. In total, each of our simulations use ~50,000 trajectories. Along each trajectory we record the matter density (ρ), temperature (T), electron fraction (Y_e), and the change in the electron fraction coming from the neutrino interactions (dY_e^ν). The electron fraction evolves along the trajectory. Some of this evolution is from the aforementioned dY_e^ν. However, the electron fraction evolution along the trajectory can also suffer from hydrodynamical mixing of the fluid, generally smoothing out the electron fraction and preventing the most neutron- or proton-rich trajectories from surviving (G. Stockinger et al. 2020). Recording dY_e^ν along the trajectory allows to us assess the impact of this. We stop the backward integration when the trajectories reach a matter temperature of 6 GK, or the beginning of the simulation. We then process each trajectory through SkyNet (J. Lippuner & L. F. Roberts 2017). We model our setup after the X-ray burst test case provided with SkyNet. This utilizes a 686 species reaction network, with over 8000 reactions between the species. For each trajectory we initialize the network with either nuclear statistical equilibrium (NSE) compositions (if the trajectory originates at a matter temperature of 6 GK) or the initial composition from the progenitor (based on the initial radius). For the NSE initial conditions we assume the Y_e of the trajectory at 6 GK while for the initial composition at the start of collapse we take the Y_e from the initial conditions. In both cases Y_e is not evolved along the trajectory within SkyNet; this is a good approximation as most neutrino interactions will happen at temperatures well above the 6 GK NSE transition temperature we choose here. The precision predictions of many isotopes (C. Fröhlich et al. 2006; M. A. Sandoval et al. 2021; J. A. Harris et al. 2017) will require a higher transition temperature and a self-consistent coupling of neutrino interactions into the nuclear reaction network.

Following the SkyNet calculation, we reduced the compositions to 20 species, plus two species to track the remaining mass. The two other species fall into two categories: "fossil" elements, which are elements more massive than ^{44}Ti present outside the silicon core in the progenitor star, and "tracer" elements, which are elements outside of our standard set of 20 elements that are produced within SkyNet in the nucleosynthesis calculation. The need of "fossil" elements is due to the available set of initial compositions in the progenitor model that do not accurately reflect the actual distribution of these fossil elements. Our initial models have $\sim 0.05\,M_\odot$ of these fossil elements, which can be considered to have a solar-metallicity distribution of elements more massive than ^{44}Ti. These species are simply advected in our post-CC simulations.

2.5. Progenitor

We use a 60 $M_\odot$ zero-age main-sequence solar-metallicity progenitor from T. Sukhbold et al. (2018) with reduced mass loss (from their $\dot{M}_{\rm N}/10$ models), resulting in a remaining mass of 47.31 $M_\odot$ by the time the core begins collapsing. This progenitor has a compactness, $\xi_{2.5} = 0.63$, and $\xi_{1.75} = 0.91$, with compactness defined as in E. O'Connor & C. D. Ott (2011a):

$$\xi_M = \frac{M/M_\odot}{R(M_{\rm bary} = M)/1000\ {\rm km}}, \quad (4)$$

and evaluated at the time of collapse. This is the highest 2.5 $M_\odot$ compactness progenitor in the compendium from T. Sukhbold et al. (2018), but it is worth noting that there are similarly compact progenitors in the 30–40 $M_\odot$ mass range. This can be seen in Figure 1 (and in Figure 8 of T. Sukhbold et al. 2018)

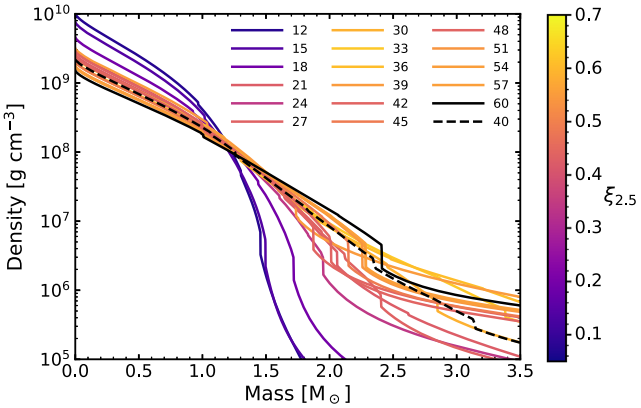


Figure 1. For several progenitors from T. Sukhbold et al. (2018), the density profiles are plotted and colored according to their compactness as defined by Equation (4) using a 2.5 $M_\odot$ mass coordinate. In black we highlight the $\xi_{2.5} = 0.63$, 60 $M_\odot$ progenitor we use in this study. We also include the $\xi_{2.5} = 0.54$, 40 $M_\odot$ progenitor from T. Sukhbold et al. (2016, dashed black line) that results in a BHSN in A. Burrows et al. (2023).

where we plot density profiles from the $\dot{M}_N/10$ compendium. We highlight the 60 $M_\odot$ progenitor used in this study with a black line. For comparison, which we return to later in Section 4, we also include a 40 $M_\odot$, $\xi_{2.5} = 0.54$, and $\xi_{1.75} = 0.87$ progenitor from T. Sukhbold et al. (2016, dashed black line). This 40 $M_\odot$ progenitor was simulated in 3D by A. Burrows et al. (2023) and resulted in a BHSN. For the 60 $M_\odot$ progenitor, there is a sharp drop in density at $\sim$2.4 $M_\odot$, which is near the bottom of the silicon/sulfur layer and does not correspond to the silicon–oxygen interface (at $\sim$6.7 $M_\odot$). Figure 2 shows the initial composition profile of the progenitor in both radius coordinate (left) and enclosed mass coordinate (right). The dashed vertical line in the left panel marks the radial coordinate ($\sim 3.4 \times 10^8$ cm) that corresponds to the $\sim$2.4 $M_\odot$ mass coordinate. In the silicon/sulfur layer, which is bounded by the iron layer from below and the oxygen layer from above, there is yet a small mass fraction of oxygen. We interpret the sharp drop in the density profile at $\sim$2.4 $M_\odot$ as the transition between the region where oxygen is being burned to silicon and the region where silicon is being burned to iron.

3. Results

3.1. Prior to Black Hole Formation

We remind the reader that our models in this work, `m0.95`, `m0.75`, and `m0.55`, are distinct from one another via the effective mass parameter in the EOS, and the model name reflects the effective mass value for symmetric nuclear matter at the nuclear saturation density. Each model undergoes successful shock revival, and the maximum shock radii pass through 400 km at $\sim$0.292 s (`m0.95`), $\sim$0.317 s (`m0.75`), and $\sim$0.346 s (`m0.55`). Shock revival times, as well as other important quantities, are summarized in Table 1. Shock revival does not occur when the silicon–oxygen interface accretes (which is located at $\sim$6.7 $M_\odot$), but is rather precipitated when the sharp density drop at $\sim$2.4 $M_\odot$ accretes, which lies deep inside the silicon layer (although some oxygen is present outside this interface; see Figures 1 and 2 and Section 2.5.)

Figure 3 shows the mean shock radius for each model, both before and after BH formation. The times of BH formation are indicated by the vertical dashed lines. We highlight that shock revival occurs even for the most thermally stiff EOS, `m0.55`, which, based on previous work, is known to be the EOS least prone to explosion (A. S. da Silva Schneider et al. 2019; O. Eggenberger Andersen et al. 2021). Lowering the effective mass increases the thermal pressure inside the PNS, such that the PNS forms less compact and contracts less rapidly. This results in a decreased release of gravitational binding energy in the form of neutrinos, and less neutrino heating, making the model less prone to explode. We attribute the successful shock revivals to the high compactness of this 60 $M_\odot$ progenitor, which has a shallow density profile. This results in a high accretion rate, which powers a high neutrino luminosity and a hard neutrino spectrum. The hard neutrino spectrum, combined with a high gain region density, results in a high optical depth in the gain region. This high optical depth, along with the high neutrino luminosity, manifest in significant neutrino heating and turbulent convection, enabling shock revival even for the most thermally stiff model.

Figure 4 shows the central density evolution. The higher the effective mass, the more rapid the central density evolves due to a decreased thermal pressure within the PNS. Owing to this thermal pressure dependence, a higher effective mass model can support a less massive PNS and collapses into a BH sooner. Model `m0.95` forms a BH at $\sim$0.93 s, model `m0.75` at $\sim$1.36 s, and model `m0.55` at $\sim$1.45 s.

From top to bottom in Figure 5, we show the electron neutrino luminosity, the electron antineutrino luminosity, the neutrino heating rate, and the mass accretion rate. The neutrino luminosities are the energy flux in the radial direction integrated over a spherical surface at 500 km. The neutrino heating is the integral over zones, with entropies above 6 k_B baryon^{-1} and densities below 3×10^{10} g cm^{-3}, that gain energy (internal plus kinetic) after a time step in the neutrino unit. The mass accretion rate is the mass per unit time that falls inward through a spherical surface at 500 km. In the figure insets we show a smoothed version of the same plots to discern trends between the models. We see that the neutrino luminosities and heating rate increase with effective mass before shock revival, such that the `m0.95` model explodes first and more energetically, and within a window of $\sim$50 ms, is followed by the `m0.75` model and then the `m0.55` model. Note also how this energy hierarchy between the models inverses after shock revival: the higher the effective mass, the more matter is ejected by the initial shock. This decreases the subsequent accretion rate, powering less neutrino emission and heating. It is important to note this energy hierarchy to fully interpret the impact of the thermal EOS, since these effects will have some correlation with the final explosion energy—a topic we revisit at the end of this section.

We observe, but omit to show with a figure, that the higher the effective mass, the higher the average neutrino energy of all species, both before and after shock revival. This occurs because the neutrinospheres are located at higher temperatures (A. S. da Silva Schneider et al. 2019). In contrast to the electron neutrino and electron antineutrino luminosities, the heavy lepton neutrino luminosity increases with the effective mass throughout. This highlights how accretion aids in fueling the emission of electron neutrinos and electron antineutrinos, while the contraction of the PNS fuels the heavy lepton neutrinos.

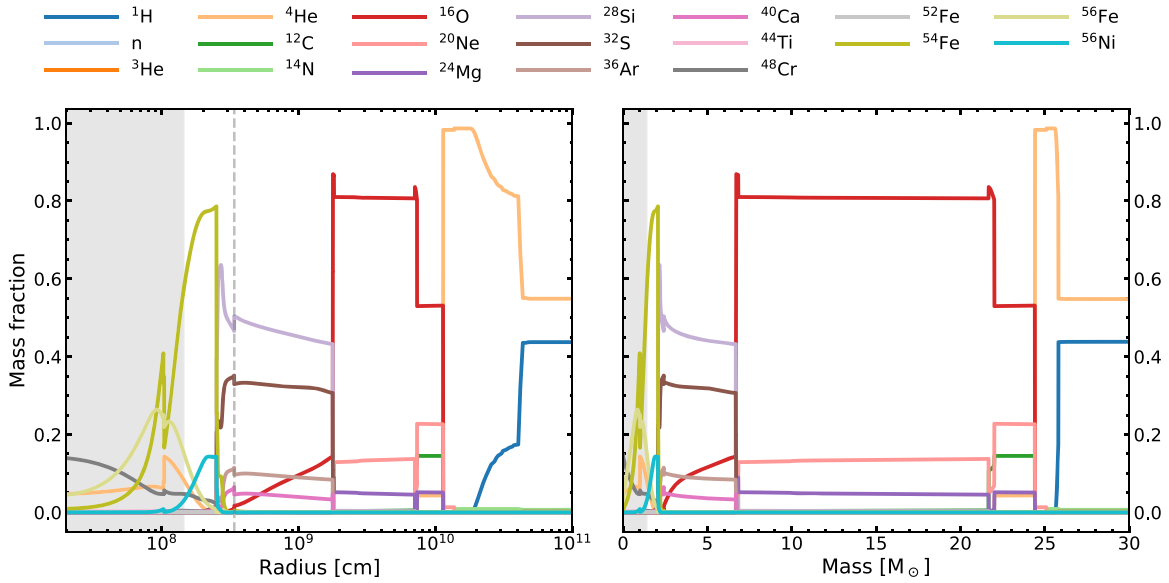


Figure 2. Mass fractions of the elements in the progenitor at the point of collapse, as a function of radius (left) and enclosed mass (right). Outside of 10^{11} cm and 30 $M_\odot$, where we limit these plots, the ^{4}He and ^{1}H mass fractions are approximately constant. The dashed vertical line at $\sim 3.4 \times 10^{8}$ cm ($\sim 2.4\ M_\odot$) in the silicon layer, corresponds to the sharp drop in the density profile in Figure 1 and marks the transition from the oxygen-burning layer to the silicon-burning layer. The shaded areas indicate regions where more than 10% of the mass consists of other species, as calculated in a quasi-statistical-equilibrium network (T. A. Weaver et al. 1978; T. Sukhbold et al. 2018).

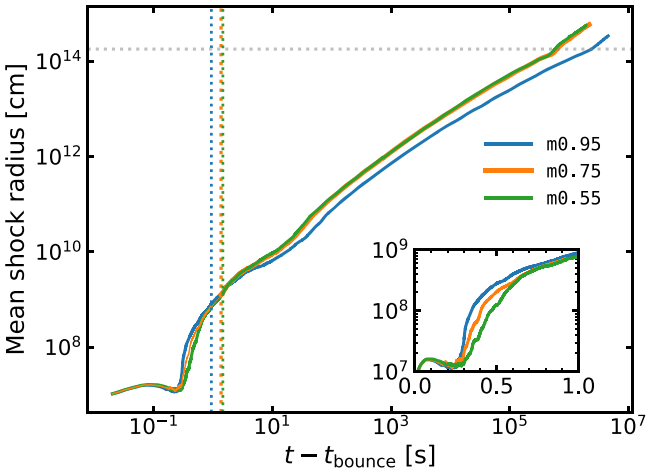


Figure 3. Mean shock radius as a function of time for the three models varying only in the effective mass parameter in the EOS. Increasing the effective mass thermally softens the EOS, increasing the explodability. The vertical dotted lines indicate the time of BH formation for each model. The horizontal line marks the surface of the star.

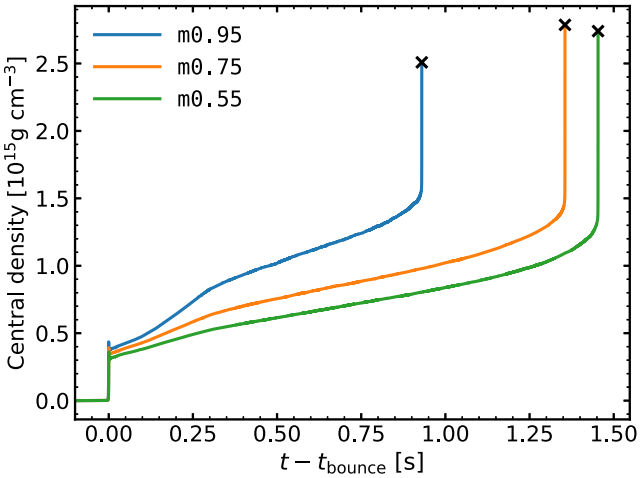


Figure 4. Central density evolution for the three models varying in effective mass. Increasing the effective mass reduces the thermal pressure, leading to a more compact PNS that contracts more rapidly, resulting in an earlier collapse to a BH. BH formation is signaled by a millisecond-scale collapse of the PNS (black crosses).

Table 1
Overview of the Simulations That Vary in the Effective Mass Parameter, $m^\star$

$m^\star$ (m_n)	$t_{\rm sr}$ (s)	$t_{\rm BHF}$ (s)	$E_{\rm expl}$ (10^{50} erg)	$M_{\rm BH}$ ($M_\odot$)	$M_{\rm ej}$ ($M_\odot$)	$M_{\rm Ni^{56}}$ ($M_\odot$)
0.95	0.292	0.93	0.57	25.48	21.67	0.000
0.75	0.317	1.36	7.23	24.02	23.09	0.0157
0.55	0.346	1.45	6.68	24.30	22.80	0.0182

Note. We report the approximate shock revival time, $t_{\rm sr}$, the time to BH formation ($t_{\rm BHF}$), the final explosion energy ($E_{\rm expl}$), the final BH mass ($M_{\rm BH}$), the ejected mass ($M_{\rm ej}$), and the ^{56}Ni ejecta ($M_{\rm Ni^{56}}$). Times are relative to core bounce.

In Figure 6, we show the commonly used diagnostic explosion energy, $E_{\rm diag}$ (R. Buras et al. 2006; B. Müller et al. 2017), with the extra condition that the radial velocity is positive (as in N. Rahman et al. 2022):

$$E_{\rm diag} = \int_{e_{\rm tot}, v_{\rm r} > 0} \rho e_{\rm tot}\, dV, \tag{5}$$

$$e_{\rm tot} = \epsilon_{\rm int} + \frac{v^2}{2} + \Phi, \tag{6}$$

where ρ is the density, dV is a volume element, $\epsilon_{\rm int}$ is the internal energy, v is the fluid velocity, and Φ is the potential energy. The dashed lines in Figure 6 are calculated using $\Phi = -{\rm G}M^{\rm grav}_{\rm encl}/r$, where $M^{\rm grav}_{\rm encl}$ is the enclosed gravitational mass at spherical radius r. As both variations of the diagnostic explosion energy are used in the literature, we include both. When using the potential, the assumption is that every unbound parcel (positive $e_{\rm tot}$) needs to "climb" out of the potential well,

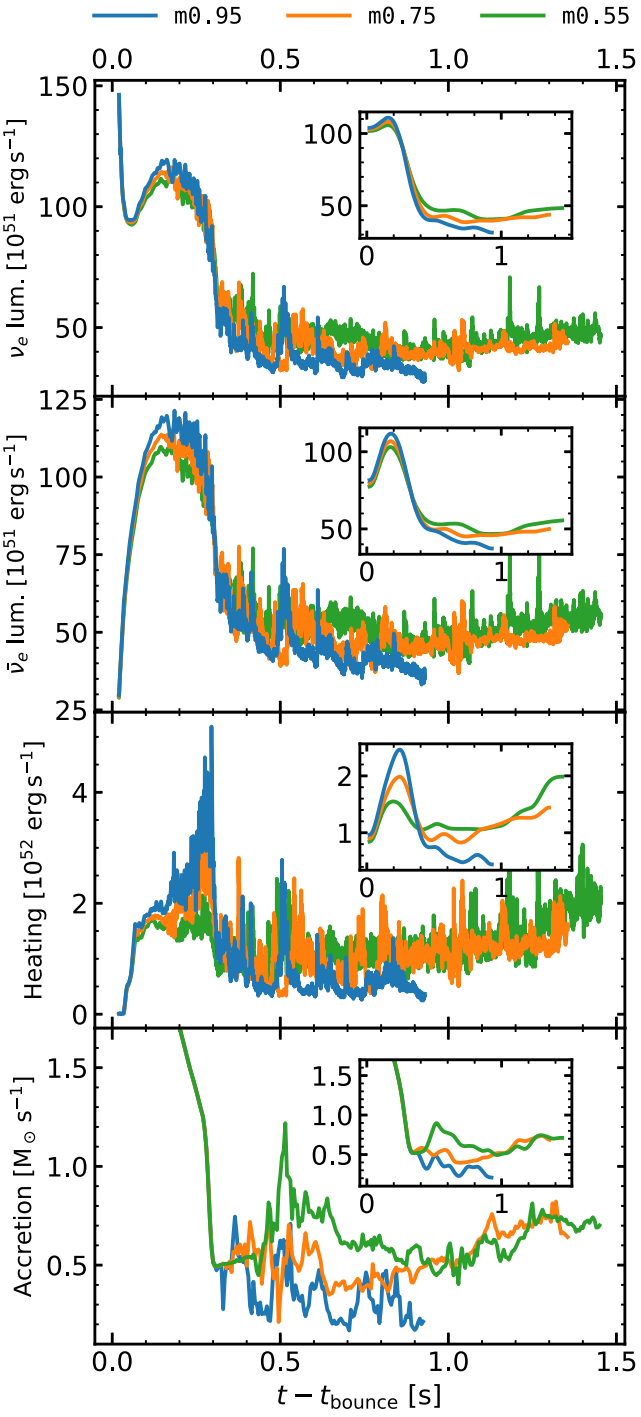


Figure 5. Top to bottom: electron neutrino luminosity, electron antineutrino luminosity, neutrino heating rate, and mass accretion rate. In the figure insets, we show a much more smooth version of the same plots to obtain a clearer view of the trends. With higher effective mass, there is an increase in the displayed neutrino quantities until shock revival, at which point this trend reverses due to the difference in mass ejection by the initial explosion.

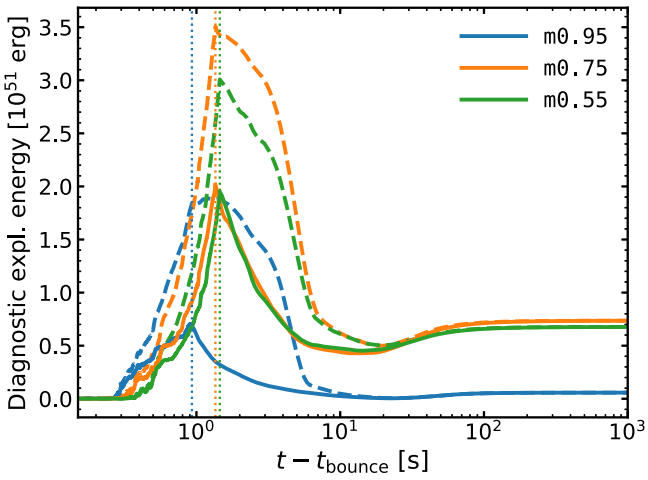


Figure 6. Diagnostic explosion energy according to Equation (5) (solid lines). The dashed lines are the diagnostic calculated by replacing the potential energy term, Φ, in Equation (5) with $-GM_{\rm encl}^{\rm grav}/r$ (see text). BH formation occurs at similar times (vertical lines) for the m0.75 and m0.55 models, resulting in similar explosion energies. In contrast, the m0.95 model experiences BH formation earlier, allowing less time to build up explosion energy via neutrino-driven winds.

taking all the mass shells outside its current radius into account. This results in a form of double counting inside the unbound region when several mass layers are unbound (B. Müller et al. 2017). In other words, a parcel is estimated to escape with an energy of $E_{\rm diag}$, but its mass still contributes to the potential when another parcel is evaluated in Equation (6). Thus, using the potential underestimates the explosion energy. Using $-GM_{\rm encl}^{\rm grav}/r$ does not take into account the mass outside radius r, avoiding double counting but overestimating the explosion energy. Both these definitions assume that unbound regions will not transfer energy to bound regions (negative $e_{\rm tot}$) that stay bound. Nor do they take into account the kinetic energy in the bound regions that can contribute to a final explosion energy (e.g., bound material that moves outward and interacts). As such they are truly only diagnostic energies and long-term simulations are needed to model the redistribution of energy. At late times and large radii, both diagnostics converge to the final explosion energy.

Before BH formation, the diagnostic explosion energy continues rising as long as the neutrinos inject energy into the matter in the vicinity of the PNS, momentarily unbinding some of that matter. Matter streams back up toward the shock front due to neutrino heating, aided by buoyancy forces since these winds are low in density while high in temperature and entropy. Neutrino-driven winds typically occur along the poles in our simulations, while the bulk accretion occurs in the equatorial plane and powers the neutrino emission. The multidimensional dynamics is crucial in enabling BHSNe events, allowing accretion to occur while the explosion develops. We further discuss dimensionality in Section 4.2. At BH formation, the neutrino engine ceases to inject energy and the conservative diagnostic explosion energies reach their peak ($\sim$0.7–2.0 $\times$ 10^{51} erg). The m0.95 model peaks at a much lower energy ($\sim$0.7 $\times$ 10^{51} erg) compared to the other two models, which are quite similar, with m0.75 peaking the highest ($\sim$2.0 $\times$ 10^{51} erg).

Based on 1D simulations, the expectation was that model m0.55 would have the highest explosion energy peak, followed by model m0.75 and then model m0.95. A lower effective mass EOS can support a more massive PNS and therefore delay BH formation. This increases the duration between shock revival and BH formation, during which the neutrino engine can build up the explosion energy. In the initial 1D simulations we performed, as well as in the 1D simulations

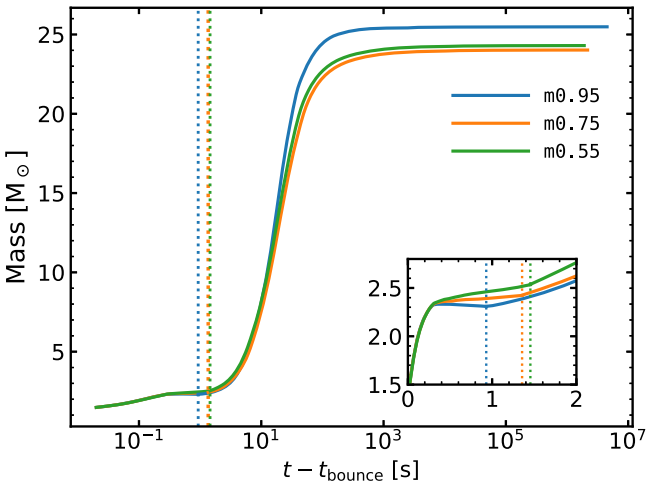


Figure 7. Gravitational mass of the compact object. The vertical lines indicate when the BHs form. The inset zooms in on the first 2 s. After shock revival, higher effective mass models accrete mass more slowly since they eject more material with the revival. $\sim 22\,M_{\odot}$ accretes onto the BHs within hundreds of seconds.

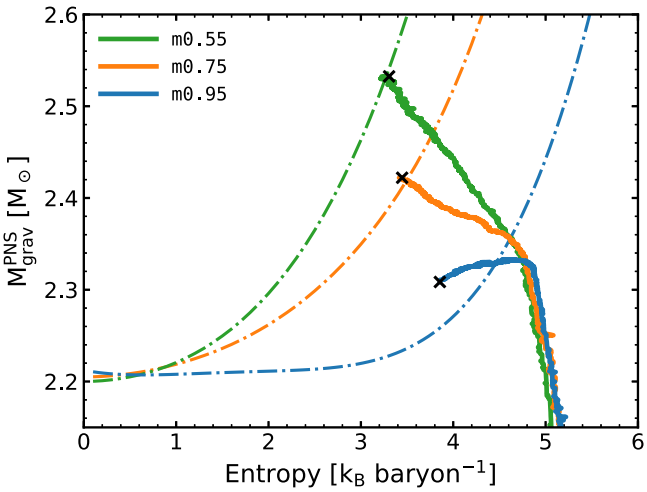


Figure 8. Gravitational mass of the PNS as a function of the most common entropy (solid lines). The dashed–dotted lines represent the maximum gravitational mass the EOSs can support given a constant entropy PNS. When the gravitational mass of the PNS reaches the maximum mass set by the EOS (at a certain entropy), collapse is expected to occur (A. da Silva Schneider et al. 2020). The black crosses indicate BH formation. After shock revival, the paths in mass–entropy space are broken. The `m0.75` model has a shallower slope than model `m0.55` due to a decreased accretion rate, delaying the time to BH formation, which impacts the diagnostic explosion energy.

by A. da Silva Schneider et al. (2020), the BH formation times increased much more linearly with decreased effective mass compared to the 2D simulations presented here. One perspective of the three different paths to BH formation was shown by the central density evolution in Figure 4 where the evolutions for model `m0.55` and model `m0.75` are more similar than in 1D. Model `m0.55` forms a BH latest at 1.45 s, closely followed by model `m0.75` at 1.36 s, while the PNS in model `m0.95` collapses at 0.93 s. To explain why this occurs in 2D and why the `m0.75` model peaks at a slightly higher energy than the `m0.55` model beyond acknowledging stochasticity[6] in SN simulations, a more in-depth analysis is required. This is presented now.

While the explosion energy is most sensitive to the duration between shock revival and BH formation, this interval is set by the compactness evolution of the PNS and is therefore dependent on the accretion rate. Given equal accretion rates, a higher effective mass model has a more rapid PNS compactness evolution. However, after shock revival, the accretion rates differ among the three models. The higher the effective mass, the more matter is initially expelled by the shock and the lower the subsequent accretion rate (recall Figure 5). This impacts the diagnostic explosion energy in two ways, which have a tendency to counter each other: (1) A decreased accretion rate slows down the PNS mass and compactness evolution, delaying the moment when the PNS reaches the maximum mass the EOS can support. Figure 7 shows the gravitational mass of the compact object evolution over time. In the figure inset, it is clear how the slope of the gravitational mass decreases when increasing the effective mass, increasing the time the neutrino engine is doing work. On its own, this has a positive impact on the explosion energy. (2) Since accretion fuels the electron neutrino and antineutrino number emission, the heating rate follows the accretion rate, which we see in Figure 5. A decreased accretion rate has a negative impact on the slope of the diagnostic explosion energy. The rapid drop in accretion for the `m0.95` model is likely causing the shallowing slope in the diagnostic explosion energy after $\sim$0.5 s (see Figure 6).

The `m0.75` model represents the middle case in compactness evolution owing to the thermal part of the EOS. Consequently, `m0.75` also stands in an intermediate position regarding the amount of matter expelled in the initial explosion, as well as the rates of accretion and heating after explosion. This model achieves a balanced combination by delaying BH formation to build up explosion energy, while maintaining a high enough accretion rate to continue to power the explosion. The result is the highest diagnostic explosion energy peak across the models. Accounting for the small shock revival time difference, the time between shock revival and BH formation only differs by $\sim$61 ms between models `m0.75` and `m0.55`.

Model `m0.55`, due to the lower effective mass, requires more mass accumulation to collapse to a BH. Compared to the other models, less matter is ejected during shock revival, resulting in a higher subsequent accretion rate. This decreases the time to BH formation and narrows the gap between models `m0.55` and `m0.75`.

We extend the perspective of delaying BH formation by showing Figure 8, where we follow A. da Silva Schneider et al. (2020) and plot the gravitational mass of the PNS as a function of the most common entropy in the PNS (solid lines). We define the most common entropy as the mass averaged entropy within a window of 2 $k_{\rm B}$ baryon^{-1} centered on the entropy with the most amount of mass. This is slightly different from the approach in A. da Silva Schneider et al. (2020) in order to achieve smooth curves in 2D. The dashed–dotted lines in Figure 8 represent the maximum gravitational mass the three different EOSs can support given a constant entropy. A. da Silva Schneider et al. (2020) showed that collapse to a BH is expected to occur when these two lines cross, which is what we see. However, compared to the other two models, model `m0.95` shows a greater deviation between the actual collapse and the line crossing. This deviation is expected for higher

[6] Several phases in CCSNe are stochastic (C. Y. Cardall & R. D. Budiardja 2015; B. Müller 2020). For example, the initial shock revival can be more or less energetic due to stochastic and chaotic factors, which affect the subsequent accretion rate.

effective mass EOSs, as their PNS entropy profiles are more variable and deviate further from being constant (A. da Silva Schneider et al. 2020). For all the models, the path in mass–entropy space is broken by shock revival since the accretion rate drops, extending the time to BH formation. Since shock revival occurs closer to the maximum mass set by the EOS for the m0.95 model, the accretion rate has less of an impact on the time between shock revival and BH formation, as compared with the lower effective mass models. The shallower slope in the m0.75 model, from the lower accretion rate, delays the moment of collapse to a time close to the BH formation time in the m0.55 model. The m0.55 model has a higher accretion rate and a steeper slope in mass–entropy space, reaching BH formation sooner than it would with a lower accretion rate.

3.2. After Black Hole Formation

Figure 9 uses 2D density plots to show the explosion morphology and development for each model (m0.95, m0.75, and m0.55, from left to right) at three different stages: BH formation (top), at ∼10 s (middle), and at ∼100 s (bottom). The green contour separates the bound ($e_{\rm tot} < 0$ in Equation (6)) and unbound regions ($e_{\rm tot} > 0$ in Equation (6)). It is the unbound regions that contribute to the diagnostic explosion energy (Equation (5) and Figure 6). At BH formation, all three explosions are dipolar, with a preference for the southern pole, especially in models m0.75 and m0.55. In 2D, explosions developing along the poles are a common outcome. That the explosion dominates along the southern pole in all three simulations is likely stochastic. Until BH formation, the bulk of accretion occurs along the equator, and, particularly for models m0.75 and m0.55, along the northern pole. Meanwhile, as accretion occurs over these solid angles, neutrino-driven outflows emerge along the other solid angles, namely the polar directions, with a stronger southern preference for models m0.75 and m0.55, setting the explosion structures at BH formation seen in Figure 9. The unbound regions have high radial velocities, internal energies, entropies, and temperatures, but are low in density. For each model, the total energy in the unbound region at BH formation corresponds to the peak in the model's (conservative) diagnostic explosion energy (see Figure 6). Since model m0.95 has the shortest time between shock revival and BH formation, its unbound regions only have $\sim 0.7 \times 10^{51}$ erg of total energy, compared to models m0.75 and m0.55 with $\sim 2.0 \times 10^{51}$ erg. After BH formation, the diagnostic explosion energies decline, in part due to these neutrino-heated regions doing work and transferring energy to surrounding bound regions, which may stay bound and eventually accrete. Furthermore, the diagnostic explosion energies are expected to decline as the shocks sweep up and unbind the gravitationally bound envelopes. Each computational zone in the envelope needs an injection of $|e_{\rm tot}|$ amount of energy to become diagnostically unbound. The middle panels in Figure 9 show how only the southern unbound region survives at ∼10 s for all three cases, and how the unbound volume is smaller for the low-energy m0.95 model. After the decline, in general, the three diagnostic explosion energies reach a minimum between ∼12 and 22 s, then rise slightly before asymptoting to a nonzero value after ∼100 s. More specifically, model m0.95 reaches its minimum at ∼22 s when the diagnostic explosion energy is 4.28×10^{48} erg, having only retained 0.6% of the peak diagnostic explosion energy. Then the diagnostic explosion energy rises and settles at a final explosion energy of 5.7×10^{49} erg, which is more than an order of magnitude higher than the minimum. This energy comes primarily from bound matter with positive radial velocity that reaches a layer in the star that is loosely gravitationally bound, unbinding it. We discuss this phenomenon in detail further down in this section and in Section 4.1. Models m0.75 and m0.55, which have higher energy budgets at BH formation and shocks that have reached further out in the "gravitational well," suffer less fractional energy losses. Model m0.75 reaches its minimum at ∼12 s when the diagnostic explosion energy is 4.28×10^{50} erg, having retained 21.4% of the peak explosion energy. After the rise, its final explosion energy is 7.23×10^{50} erg. Model m0.55 reaches a minimum at ∼14 s when the diagnostic explosion energy is 5.52×10^{50} erg, having retained 23.6 %. Its final explosion energy is 6.68×10^{50} erg.

The EOS dependence is also manifested in the ejecta mass and the final BH mass (see Figure 7). Model m0.95, which has the smallest time interval between shock revival and BH formation and the lowest explosion energy, ends up accreting more than 1 $M_\odot$ of additional matter onto the BH compared to the other two models. The final BH (ejecta) masses are 25.5 (21.7), 24.0 (23.1), 24.3 (22.8) $M_\odot$ for m0.95, m0.75, and m0.55, respectively. See also Table 1.

Figure 10 shows an animation of nearly the entire simulation for model m0.55. This animation is available in the HTML version of the article and can be accessed by clicking on the figure in the online version. The animation is made from a sequence of 2D density plots and begins at 20 ms postbounce and ends at 22.1 days. The left panel captures the evolution on a larger scale, while in the right panel focus is on the compact object. The animation illustrates how the neutrino-driven winds are ejected along the poles after shock revival, while accretion occurs along the equator. The moment of BH formation is evident at ∼1.45 s by the masking of the central region. After BH formation, the evolution of the unbound region (the diagnostic ejecta) is shown via the green contours. At ∼1 day an ingoing reverse shock is clearly visible, accompanied by bullet-like structures due to Rayleigh–Taylor instabilities (K. Kifonidis et al. 2003). The shock in the southern region starts penetrating the surface of the star at ∼3.8 days, and at ∼12 days shock breakout has occurred along all solid angles. The static version of the animation shows the explosion morphology at ∼7 days (left panel) and how the ingoing reverse shock is about to merge with itself (right panel).

The period between ∼10 s and ∼100 s, during which the diagnostic explosion energy increases, represents an interesting phase in the development of the explosion as the shock propagates through the envelope. The middle and bottom panels (at ∼10 s and ∼100 s, respectively) in Figure 9 illustrate how, during this time, the unbound regions spread from the southern hemisphere to the northern hemisphere. For model m0.55, the spread of the unbound region is dynamically shown in the online animated version of Figure 10. In general, the rise in each diagnostic explosion energy occurs because bound matter with positive radial velocities can still do work on unbound matter (while becoming "more bound" itself), as concluded by C. Chan et al. (2018). Preceding this process, bound matter with positive radial velocity can do work on itself, separating into bound and unbound regions. The onset of these processes is seen around 10 s in the middle panels of Figure 9—notice the arrow-shaped features at the leading

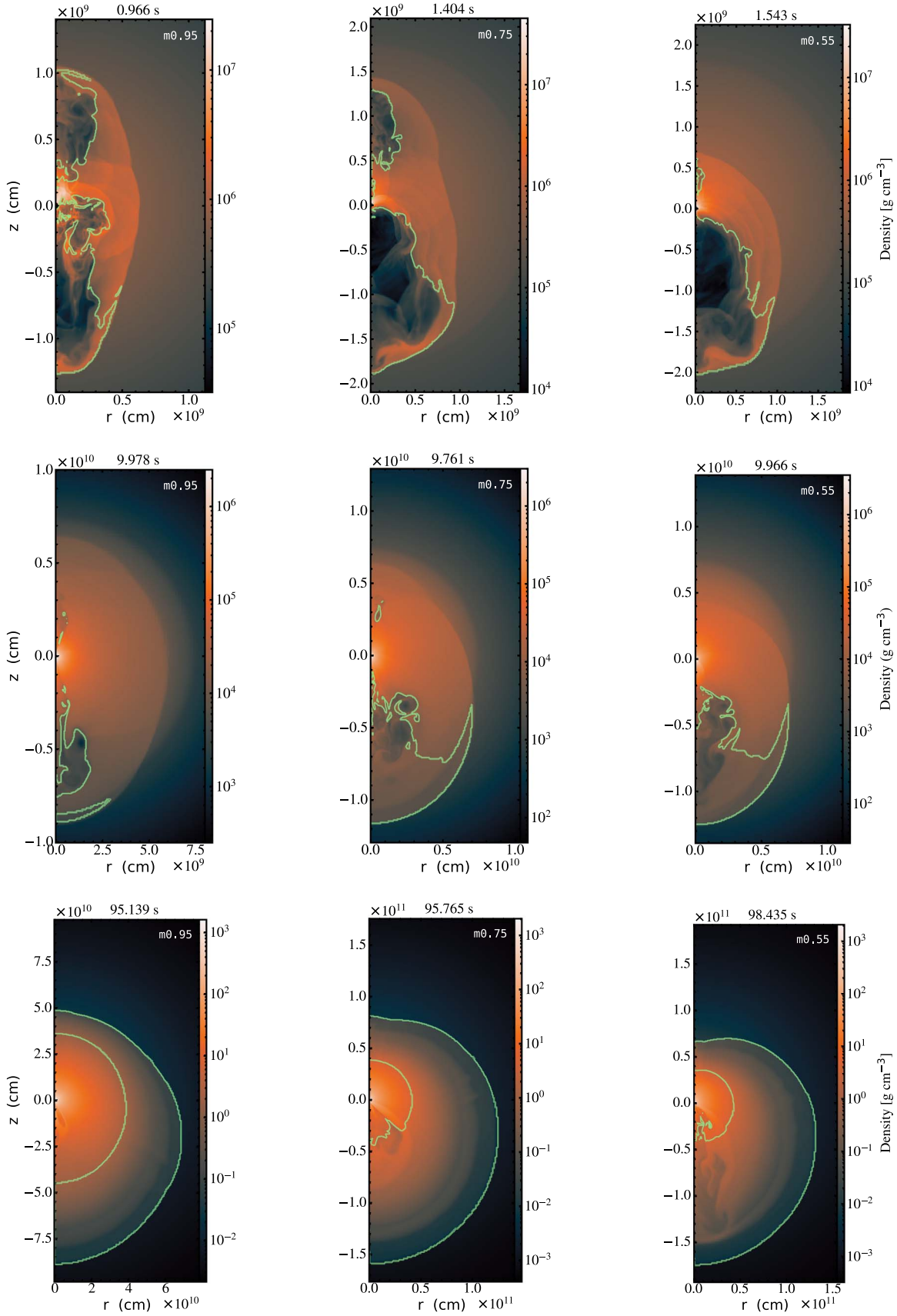


Figure 9. Density plots showing the explosion morphology and development for each model (`m0.95`, `m0.75`, and `m0.55`, from left to right) at three different stages: BH formation (top), at ∼10 s (middle), and at ∼100 s (bottom). The green contour separates the bound and unbound regions and demonstrates how the southern unbound region survives and spreads to the northern hemisphere. Note that the scale for the `m0.95` model is generally smaller than for the other two models.

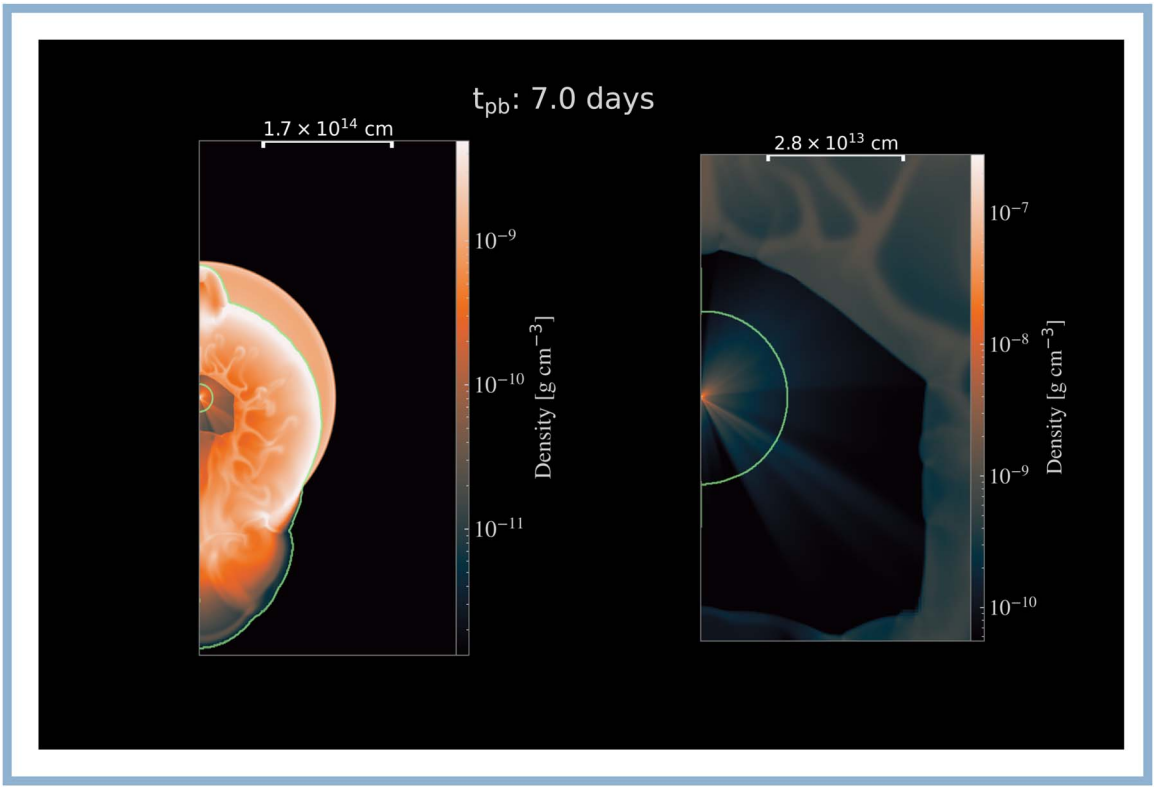


Figure 10. A snapshot of the density field (at 7 days after CC) from an animation that illustrates the evolution for model `m0.55` between 20 ms postbounce and 22.1 days. The left panel captures a larger field of view and follows the evolution of the shock, while the right panel emphasizes the area closer to the compact object. The animation illustrates how the standing accretion shock instability (J. M. Blondin et al. 2003) and turbulent convection aid in shock revival around 346 ms. Proceeding shock revival, the bulk of the accretion occurs along the equator while neutrino-driven winds are ejected along the poles (particularly in the south), creating an asymmetric explosion morphology. The PNS collapses into a BH at ∼1.45 s. After BH formation, the evolution of the unbound region (the diagnostic ejecta) is shown via the green contours. During the first ∼12.5 s after BH formation, energy is drained from the neutrino-heated bubbles. Although the shock moves outward in all directions, only the southern unbound region stays unbound until the shock enters a low-density neon/oxygen layer. At this point, the unbound region spreads from south to north (see text for details) and the diagnostic explosion energy increases (see Figure 6). At ∼1 day, an ingoing reverse shock is clearly visible, accompanied by bullet-like structures resulting from Rayleigh–Taylor instabilities (K. Kifonidis et al. 2003). The shock in the southern region starts penetrating the surface of the star at ∼3.8 days, and at ∼12 days shock breakout is completed along all solid angles. The static version of the animation shows the explosion morphology at ∼7 days (left panel) and how the ingoing reverse shock is about to merge with itself (right panel).
(An animation of this figure is available in the online article.)

shock front. Around 10 s, the leading shock fronts in the southern hemisphere have just entered a low-density layer in the progenitor. Lower-density material requires less energy to unbind. The shocks are asymmetric, and as they sequentially enter the low-density layer, the unbound regions spread from south to north. The `m0.95` model, in particular, for which the diagnostic explosion energy increases by a factor of ∼10, demonstrates how the kinetic energy in the outgoing bound matter is sufficient to overcome the binding energy in that layer (and beyond). At ∼100 s the unbound region has sphericalized in all models, and the diagnostic explosion energy has settled on its final value.

To tie the evolution of both the shock and the unbound region to the progenitor structure, we show the ρr^3 profile as well as the radial velocity of the maximum shock radius as it passes through the progenitor in Figure 11 (for the `m0.95` model). The shock speed responds to the density structure of the progenitor (L. I. Sedov 1959; K. Kifonidis et al. 2003), increasing (decreasing) when the ρr^3 profile decreases (increases). We also plot the unbound volume as a fraction of the spherical volume spanned by the maximum shock radius (as a function of the maximum shock radius). The fractional unbound region size decreases until the maximum shock radius reaches the sharp drop in density at the O–Ne/C interface (at $\sim 22\,M_\odot$, see

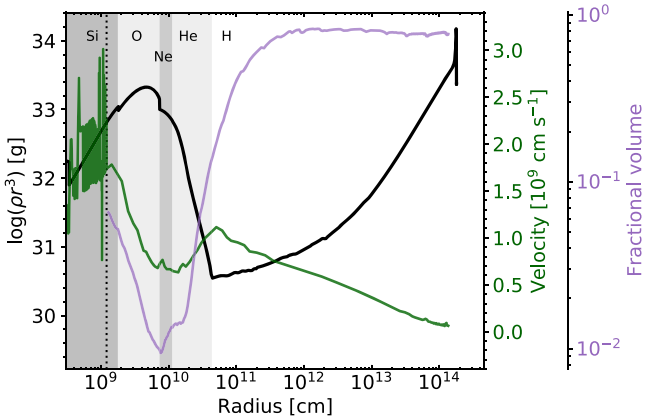


Figure 11. ρr^3 profile of the progenitor (black), the radial velocity of the maximum shock radius (green), as well as the fractional volume of the unbound region (purple) for the `m0.95` model. The volume is given as a fraction of the spherical volume spanned by the maximum shock radius. Shells are highlighted with shaded bands. The dashed line marks the maximum shock radius at BH formation.

Figure 2). At that point, the fractional unbound volume reaches its minimum and then starts increasing, spreading across the shock front as the shock front sequentially reaches the interface

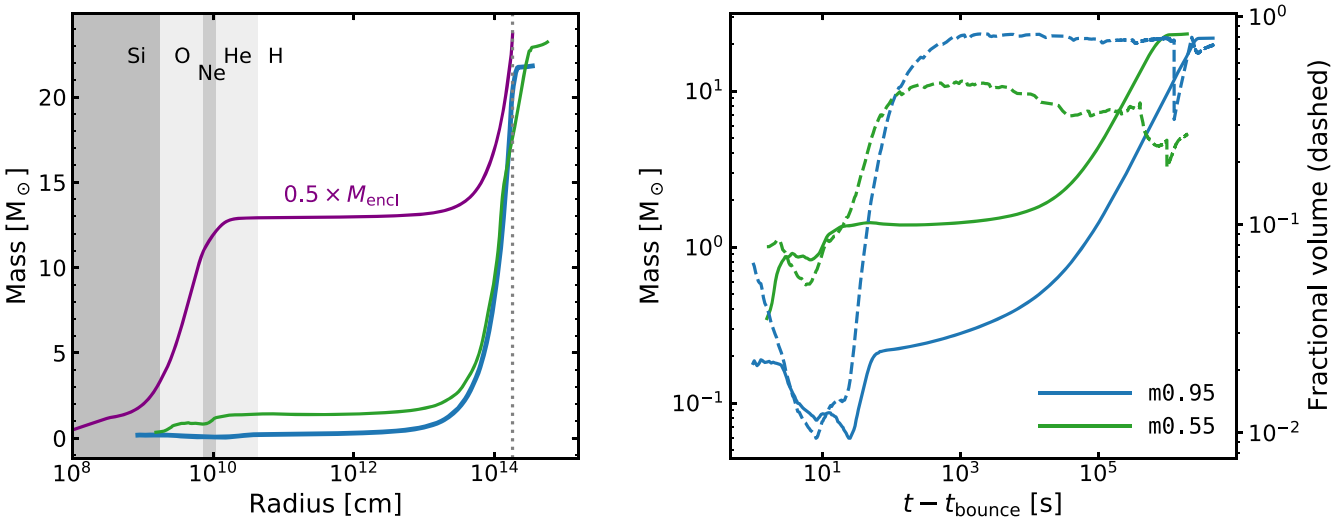


Figure 12. Left panel: enclosed mass (purple; multiplied by 0.5) and the unbound mass for `m0.95` and `m0.55` as a function of where the maximum shock radius is. The dotted vertical line marks the edge of the star. Right panel: unbound mass as a function of time (solid lines) and the fractional volume of the unbound region (dashed lines; see Figure 11). This figure highlights how the unbound mass and volume correlate and are affected by the progenitor structure. During the first ∼20 s, before the unbound regions sphericalize above the O–Ne/C interface, the unbound regions suffer mass losses, particularly in the low-energy model `m0.95`. The unbound "bubbles" carry $\lesssim 1\,M_\odot$ from depths where the binding energy is comparatively high—below the O–Ne/C interface. Above this layer, between 10^{11} and 10^{13} cm, the enclosed mass is nearly constant. All models sweep up the outermost, loosely bound, ∼21.5 $M_\odot$. In model `m0.55`, due to its higher energy compared to model `m0.95`, an additional ∼1.1 $M_\odot$ is brought from low radii before the unbound region spreads along all solid angles and the sweeping phase begins.

layer. This is a case of bound matter separating into bound and unbound regions, explaining the rise in the diagnostic explosion energy after ∼22 s. Furthermore, pressure equalization from the high internal energy and high-pressure unbound regions can act much more readily once on the low-density side, which also contribute to the spread of the unbound region. When this happens, we witness a mass flux behind the shock from south to north. Again, this is common in all models.

In Figure 12 we highlight the impact of the progenitor structure on the unbound mass for models `m0.95` and `m0.55`. The unbound mass can be thought of as the diagnostic ejecta. The right panel shows how the unbound mass as a function of time (solid lines) correlates with the fractional unbound volume evolution (dashed lines), and the impact of the density drop at the O–Ne/C interface on both quantities. In the left panel, the unbound mass is shown as a function of radius (where the maximum shock radius is), and we also include the enclosed mass of the 1D progenitor (purple). When the shock is at $\sim 10^{11}$ cm (around ∼100 s) and the BH masses have nearly asymptoted at ∼24–25 $M_\odot$ (see Figure 7), the explosion energy is carried by only ∼0.2 $M_\odot$ and ∼1.4 $M_\odot$ for models `m0.95` and `m0.55`, respectively. Then slowly, and once the unbound region has spread along all solid angles, the shock easily sweeps up the loosely bound hydrogen envelope of the star. The final ejecta mass for model `m0.95` is ∼21.7 $M_\odot$, while model `m0.55` ejects ∼22.8 $M_\odot$. The ∼1.1 $M_\odot$ difference in the final ejected mass originates from more swept-up matter before the O–Ne/C interface for model `m0.55`, as well as smaller mass losses before and shortly after crossing that region. The aforementioned mass losses can be seen in the right panel of Figure 12 before ∼20 s. The EOS dependence of the ejected mass would be significantly more pronounced if the hydrogen envelope of this progenitor was smaller.

3.3. Ejecta Composition

We aim to follow the evolution of the elemental distribution in the unbound material behind the shock front and understand the impact of BH formation on this diagnostic ejecta. Recall that we define a cell to be unbound if the total energy is above zero, or, equivalently, $e_{\rm tot} > 0$ in Equation (6). We choose the more conservative measure of $e_{\rm tot}$ by using the potential and not $\Phi = -GM_{\rm encl}^{\rm grav}/r$ in Equation (6) (see Section 3.1). At late times and large shock radii, both measures converge.

In Figure 13 we show the elemental distribution in the unbound region (solid bars) and of the entire domain (transparent bars; which includes the 2.1 $M_\odot$ atmosphere tagged as neutrons) for all three models at BH formation and after masking. We show the α-chain elements, and combine other species into a tracer element. We have checked that the act of masking has no effect on the ^{56}Ni mass on the domain. At the respective times of BH formation, the three models, [`m0.95, m0.75, m0.55`] have [0.130, 0.088, 0.061] $M_\odot$ of total ^{56}Ni on the domain, of which [0.061, 0.058, 0.053] $M_\odot$ is in the unbound region. In other words, the higher the effective mass, the more ^{56}Ni has been produced since more mass reached the conditions for NSE in the shock revival phase. There is, however, initially after BH formation, a similar amount of ^{56}Ni in the models' respective unbound regions. To advect this ^{56}Ni beyond BH formation is a very good approximation since an inconsequential amount of ^{56}Ni is produced after BH formation. We demonstrate this in the Appendix where, for positions of interest at the time of BH formation, we show the thermodynamic properties along their backward-traced and forward-extrapolated trajectories on the domain, as well as the evolution of the He^4 and ^{56}Ni abundances.

Figure 14 shows the evolution of the ejecta composition (the unbound region behind the shock front) from BH formation to 52.3 days for the `m0.95` model (right panel) and 22.1 days for the `m0.55` model (left panel). At these times, the shock for the `m0.95` model is still at a lower radius compared to `m0.55`, but all models are well beyond shock breakout and their ejecta compositions are asymptoted. We omit to show such a plot for `m0.75`, since this model is qualitatively and quantitatively

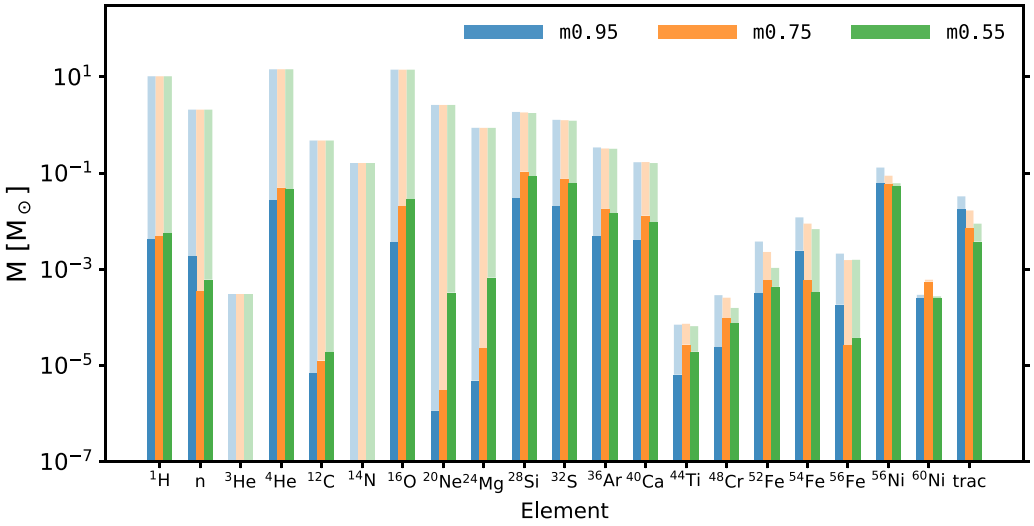


Figure 13. Elemental composition in the unbound region (solid bars) at the time of BH formation. For comparison, we also include the matter within the entire domain (transparent bars).

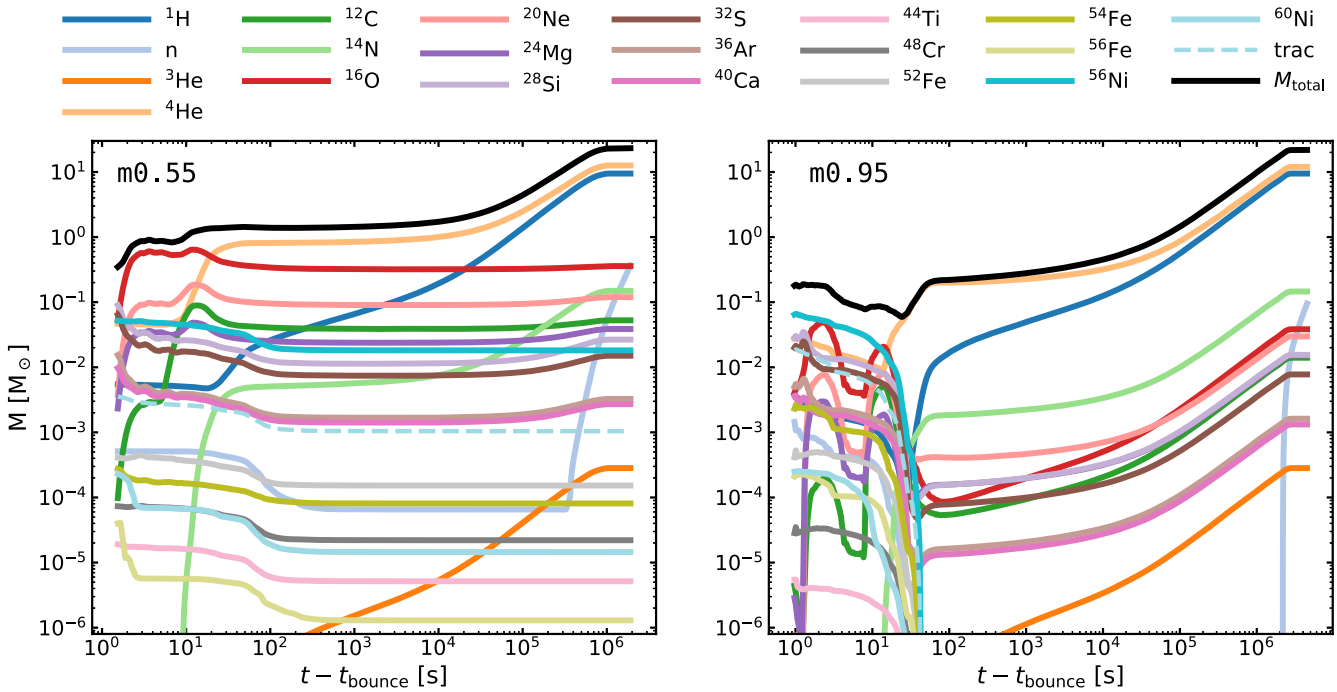


Figure 14. Elemental composition (colored lines) and the total mass (black lines) of the ejecta after BH formation for the `m0.55` model (left) and the `m0.95` model (right). A lot of variability is seen between 1 and 100 s as the high-energy unbound regions interact with bound regions. In this time interval, these evolution curves showcase the interplay between the mass-increasing effect of the shock sweeping up material, and the mass-decreasing effect of matter leaving the unbound region from below (e.g., the double peaks, see text). For some elements, such as the explosive nucleosynthesis element ^{56}Ni, there is no additional mass to sweep up as the shock propagates, and a fraction accretes onto the BH. Nearly all the explosively produced elements accrete for the `m0.95` model, whereas ∼0.018 $M_\odot$ escapes in the `m0.55` model. The rise of the neutron content around 10^6 s is because of the neutron atmosphere we artificially placed outside the star to continue the evolution past shock breakout. See text for further details.

similar to the `m0.55` model. These composition curves demonstrate the effect of BH formation on the final ejecta. We see that the fraction of the initially unbound matter that continues to stay unbound after BH formation in this progenitor is mainly dictated in the first ∼300 s. This can be seen particularly well by looking at the species without any additional mass reservoir in the layers outside the shock at BH formation (like the ^{56}Ni produced in the explosion), that simply declines and settles at a value that is primarily dictated by the explosion energy at BH formation. Other factors can enter too, such as how far out of the potential well the ejecta have reached when the pressure support from below ceases at BH formation. In general, the closer the shock is to the O–Ne/C interface (see Section 3.2 and Figures 11 and 12), the lower is the impact of BH formation on the ejecta. For the `m0.95` model, with the earliest BH formation time and lowest peak explosion energy, many elements undergo a much more significant drop in unbound mass over the initial 100 s, compared to the other two models. The elements that we impose to have no additional reservoirs in the outer layers (see Section 2.4), ^{44}Ti–^{60}Ni, drop below the plot bounds and essentially reach zero.

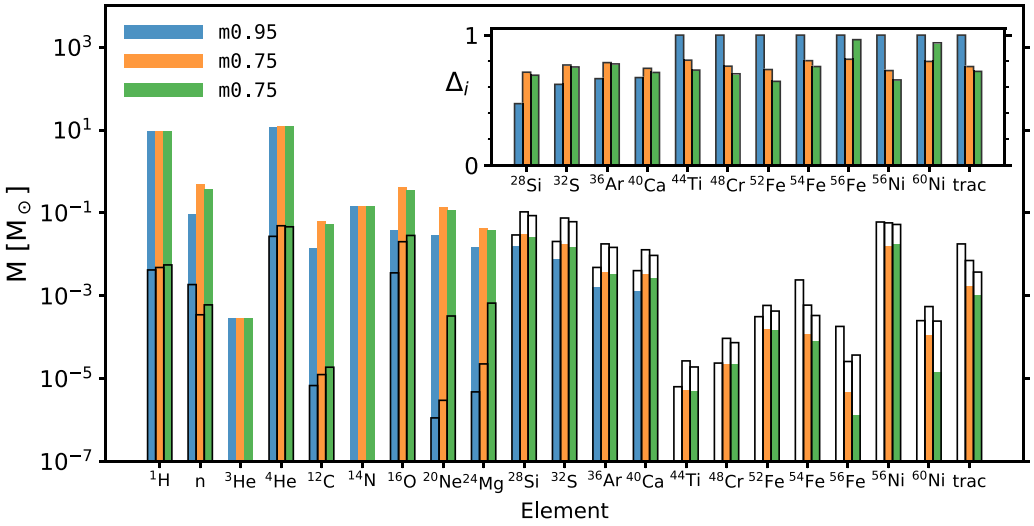


Figure 15. The final composition of the ejecta (solid bars) and the initial composition in the unbound region at BH formation (hollow bars). The inset shows the fraction of mass that is lost (Equation (7)) after BH formation. Elements H^{1}–Mg^{24} gain in mass after BH formation, whereas elements Si^{28}–Ni^{60} decrease in mass. Model `m0.95` essentially loses all of the ^{56}Ni that was initially unbound, whereas models `m0.75` and `m0.55` lose 73% and 66%, respectively. The EOS dependence of the ^{56}Ni significantly affects the electromagnetic signal.

The first hundreds of seconds also demonstrate how there is one rate of binding matter after BH formation, and one rate of the shock sweeping up new material. To see this, note the double peaked shapes of the `m0.95` model for, e.g., the ^{16}O. Our interpretation of this phenomenon is as follows. The first peak occurs because the shock and unbound region moves into the ^{16}O layer that is also enriched by ^{20}Ne, ^{24}Mg, and some ^{12}C (especially further out in this shell; see Figure 2). Then there is a general loss of mass and volume in the unbound region. At ∼8 s, a local minimum in the total mass and for, e.g., ^{16}O occurs, and is concurrent in time with when the maximum shock radius enters the low-density region above the O–Ne/C interface mentioned in Section 3.2 and Figure 11. Entering this region, when matter is easily unbound, allows for the second peak. Note that the ^{12}C increases considerably at the second peak and how this corresponds to the enhanced carbon reservoir in the layer above the O–Ne/C interface at $\sim 10^{10}$ cm (see Figures 2 and 11). While the unbound region is spreading as it passes through the oxygen-poor helium layer between ∼20 and 100 s, mass loss from below still occurs. Consequently, the ^{16}O mass decreases (as does many other elements), while the ^{4}He content of the ejecta increases. When the unbound region has sphericalized after ∼100 s, the matter has, to a high degree, separated itself into what is to become ejected and what is not, and the phase of predominantly sweeping up matter follows. During this phase, helium and hydrogen are mostly swept up, constituting the majority of the final ejecta. We see that trace elements corresponding to solar metallicity starting conditions are also swept up. This is particularly evident beyond ∼100 s in the right panel of Figure 14, when the mass for several elements heavier than neutrons (due to the artificial atmosphere), hydrogen, and helium slowly increases. Since the helium/hydrogen envelope constitutes the bulk of the ejected mass, we use this mass cut to roughly estimate an ejection of 0.03 $M_{\odot}$ of "fossil" elements (see Section 2.4) for each model.

Model `m0.55` shows similar overall dynamical behavior for the ejecta composition (left panel of Figure 14) as the `m0.95` model. However, the composition curves are less variable. The higher peak explosion energy, combined with the shock reaching the O–Ne/C interface sooner, results in a lower relative impact on the unbound mass and the individual elements. The net unbound mass loss stops completely once the shock front enters the low-density regime, although elements such as ^{16}O still become bound from below. While model `m0.95` looses nearly all its ^{16}O in the first 100 s, model `m0.55` has ∼0.64 $M_{\odot}$ of unbound ^{16}O at the peak around 12 s and loses about half of it. Similar statements comparing the two models can be made for all other elements except ^{4}He and ^{1}H. As such, even with the vast ∼20 $M_{\odot}$ of oxygen in this progenitor, only a few tenths of a solar mass of oxygen is ejected for `m0.55`, and even less for `m0.95` (essentially only the accumulated solar-metallicity elements). Generally, the unbound regions remain in a bubble shape as they pass through the relatively high-density ∼20 $M_{\odot}$ oxygen layer. They sphericalize only afterward in the helium layer. Thus, not a large fraction of the available oxygen is swept up. Most of the oxygen core accretes onto the BH instead.

Figure 15 shows the final composition of the ejecta after shock breakout for each model (solid bars; i.e., the last snapshot in Figure 14). We also include the initial unbound ejecta (hollow bars; i.e., the first snapshot in Figure 14). The figure inset displays the absolute fractional change in unbound mass between these two times:

$$\Delta_i = |(X_i^{\rm end} - X_i^{\rm start})/X_i^{\rm start}|, \quad (7)$$

where $X_i^{\rm start}$ and $X_i^{\rm end}$ are, respectively, the initial and final unbound masses for species i. Only the elements that lose mass are shown in the inset. In general, the figure shows that elements from ^{1}H–^{24}Mg gain in mass, whereas ^{28}Si–^{60}Ni decrease in mass after BH formation. Model `m0.95` loses nearly all the mass associated with the heavier species, ^{44}Ti, ^{48}Cr, ^{52}Fe, ^{56}Fe, ^{56}Ni, and ^{60}Ni. In contrast, models `m0.75` and `m0.55` retain between 20% and 35% of the initially unbound matter for these species. We comment particularly on the EOS dependence of the ^{56}Ni, as this affects the electromagnetic signals of these events. Recall that the models [`m0.95`, `m0.75`, `m0.55`] produced [0.130, 0.088, 0.061] $M_{\odot}$ of total ^{56}Ni on the domain, but had a very similar amount in the initial

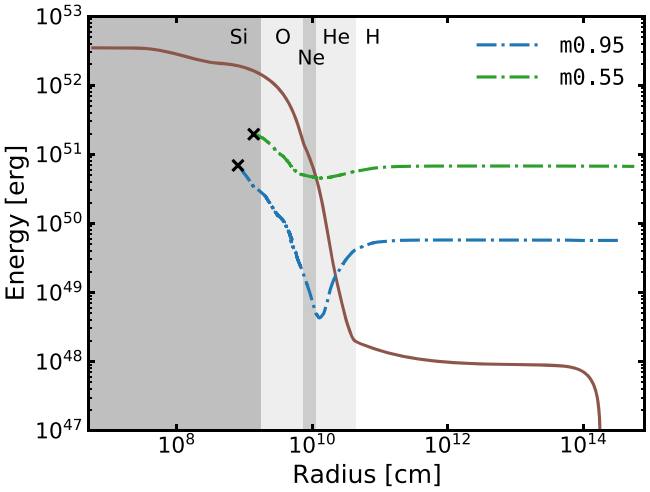


Figure 16. The absolute value of the cumulative binding energy of the progenitor from the edge of the star and inward (brown line), and the diagnostic explosion energy as a function of where the mean shock radius is for models `m0.95` (blue line) and `m0.55` (green line). At BH formation (black crosses), the binding energy outside the shock is more than 10 times the diagnostic explosion energy.

unbound region. The final unbound ^{56}Ni mass for the three models are [0.0000 (10^{-17}), 0.0157, 0.0182] $M_\odot$, meaning that practically all of the produced ^{56}Ni in the `m0.95` model accrete onto the BH, whereas 73% and 66% of the initially unbound ^{56}Ni accrete for `m0.75` and `m0.55`, respectively.

4. Discussion

4.1. The Explosion Energy Budget

The core of the 60 $M_\odot$ progenitor we use is massive and compact. In the simulations presented here, at BH formation, the diagnostic explosion energies are at least a factor of ∼10 lower than the binding energy of the material outside the shock. Similar energy imbalances are seen in simulations from J. Powell et al. (2021) and N. Rahman et al. (2022). Figure 16 shows the absolute cumulative binding energy of the progenitor from the surface of the star inward (brown line). The green and blue lines represent the diagnostic explosion energies as a function of the mean shock radius for models `m0.95` and `m0.55`, respectively. Only outside the neon layer at $\sim 10^{10}$ cm, around 10 s after shock revival, do the binding energy and the diagnostic explosion energies become comparable. A natural question to pose, then, is how the explosion survives through the massive overburden?

The unbound region in model `m0.55` exits the relatively high binding energy oxygen core with 23.6% of its initial energy at BH formation. This is a significant amount considering that the binding energy outside the shock at BH formation ($\sim 1.62 \times 10^{52}$ erg) exceeds by far both the diagnostic explosion energy ($\sim 1.95 \times 10^{51}$ erg) and the kinetic energy of bound outward-moving matter ($\sim 7 \times 10^{49}$ erg). We reason that since most of the explosion energy is concentrated in the southern region until ∼50 s, this bubble of energy does not have to face all of the overburden and transfer all of its energy. Instead, ∼22 $M_\odot$ accretes onto the BH within ∼100 s (see Figure 7) while there is still only ∼1 $M_\odot$ in the unbound region at this time (see Figure 12). Once the region with comparably high binding energy is passed, the energy in the unbound region can spread across all solid angles on the other side of the O–Ne/C interface. When this happens, we witness a mass flux from south to north. Only when the unbound region sphericalizes, and the phase of sweeping up matter begins, does the unbound region "face" all of the remaining binding energy.

It is plausible that a shock alone can move outward in mass coordinate and unbind the loosely bound envelope even with a massive overburden. While the neutrino-heated bubbles in model `m0.95` aid the propagation of the shock, the rise in the diagnostic explosion energy (after having lost 99.4%) is due to kinetic energy behind the shock. It is interesting to note that at BH formation, model `m0.95` has $\sim 8 \times 10^{49}$ erg of bound matter moving radially outward, close to the $\sim 6 \times 10^{49}$ erg rise in the diagnostic energy when the shock passes the O–Ne/C interface. Model `m0.95` motivates speculation on scenarios where no parcels with positive energy survive through the overburden (see also N. Rahman et al. 2022). However, once the shock enters into the low-potential energy regime, bound outgoing fluids can give rise to a positive explosion energy by separating into ejecta and eventual fallback material, similar to neutrino-induced mass ejection scenarios (e.g., D. K. Nadezhin 1980; R. Fernández et al. 2018). The `m0.95` model appears very close to such a case, retaining only 0.6 % of the energy in the unbound region after BH formation, until the kinetic energy increases the diagnostic explosion energy by a factor of ∼10 (see Section 3.2). Still, model `m0.95` ejects 21.67 $M_\odot$. The uncertain outcomes in J. Powell et al. (2021), B. Sykes et al. (2023), and to some extent N. Rahman et al. (2022; see Section 1) are interesting in the light of this discussion. A question that remains is, what dictates whether the shock survives or not? J. Powell et al. (2021) suggested that the shock survives if it has reached the sonic point of the infalling matter at BH formation. The simulations in B. Sykes & B. Müller (2024) are consistent with this hypothesis.

4.2. From Two Dimensions to Three Dimensions

SNe are inherently 3D, and it is important to understand how moving from 2D to 3D affects the results. In 3D, compared to 2D, there is more fine structure, with smaller but more numerous neutrino-heated bubbles and accretion funnels. This geometry can suppress the accretion rate in 3D (B. Müller 2015, 2020; A. Burrows & D. Vartanyan 2021), and therefore act to delay the BH formation time, allowing for the explosion energy to build up longer. However, the lower accretion rate could reduce the slope of the diagnostic explosion energy, competing with the aforementioned effect. Furthermore, 2D models tend to explode more energetically during shock revival (H.-T. Janka et al. 2016), acting to decrease the subsequent accretion. 3D simulations are required to see which effects dominate over the other within the ∼1.5 s window we are interested in here. J. Powell et al. (2021) in 3D and B. Sykes et al. (2023) in 2D simulate a high-compactness ($\xi_{2.5} = 0.86$), 85 $M_\odot$ progenitor, where BH formation occurs 100 s of ms after shock revival. The times of shock revival and the times of BH formation are very similar between the two studies, but the peak explosion energy is ∼30 % lower in the 2D simulation. We have simulated the same 40 $M_\odot$ progenitor in 2D as A. Burrows et al. (2023) use in their 3D simulation. The time of shock revival is similar in our simulation and in the A. Burrows et al. (2023) simulation, but BH formation occurs 200 ms earlier in our case. We intend on reporting more details on this simulation, as well as simulations of progenitors spanning a wider mass range, in future work.

Another interesting follow-up to this work is to include rotation since $\sim 22\,M_\odot$ accretes within the first 100 s, after which the accretion rate scales as the predicted $t^{-5/3}$ (R. A. Chevalier 1989). This can power outflows and affect the transient via disk formation around the BH. Even for zero net angular momentum models, modeling the stochastic build up of angular momentum can result in a disk (E. Quataert et al. 2019). Here, however, we encounter a limitation of this study due to the axisymmetric assumption where stochastic angular momentum cannot be built like in 3D, which yields interesting features in A. Burrows et al. (2023) even with their much lower accretion rate.

4.3. Final Remarks

It remains an open question of how viable BHSNe are and the mapping relation between progenitors and these outcomes. The mapping is likely mainly a function of the density profile at the time of CC. If these events are realized in nature for stars that constitute a significant fraction of the distribution of the final density profiles, they influence the compact object mass distributions as well as the galactic chemical evolution. Ideally then in the future, BHSNe will also be accounted for in population synthesis calculations.

The simulations presented here probe the importance of accretion to fuel the explosion. They hint that even in non-BH-forming scenarios, one may end up with a higher final explosion energy if the initial explosion at shock revival is less energetic, given otherwise similar conditions. If the post-shock-revival accretion rate is decreased by a high-energy explosion, less gravitational binding energy is released as a whole to continue fueling the explosion via winds.

5. Conclusions

Through three 2D simulations of a high-compactness $60\,M_\odot$ progenitor, we have explored a recently established BH formation channel, where the BHs have formed between $\sim$0.64 s and $\sim$1.11 s after shock revival. At these times, the shock waves are still inside the silicon layer, yet all have culminated in successful SNe. In these explored scenarios, it is the continued accretion of the progenitor that pushes the PNS above its maximum mass, and not fallback material as in fallback SNe. In contrast to fallback SNe, there is a large impact on the explosion dynamics. This motivates placing this BH formation channel in a category of its own, and we refer to them as BHSNe in this paper. At BH formation, we excised the central regions while accounting for the accreted mass and followed their evolution for at least 22 days postcollapse. This period extends beyond shock breakout and into a regime where the ejecta composition has settled on its final values.

We have studied the thermal EOS dependence of BHSNe by varying the effective mass of nucleons, following A. S. da Silva Schneider et al. (2019). We find a strong EOS dependence on the explosion dynamics, the mass of the BH remnant, the ejecta mass, and its composition. This highlights the importance of the EOS in these events. Increasing the effective mass, $m^\star$, yields a lower thermal pressure, which results in a faster BH formation time. This is particularly evident when comparing the `m0.95` model ($m^\star = 0.95$) to the other two. The PNS in model `m0.95` collapses to a BH at $\sim$0.93 s after bounce, at which point the diagnostic explosion energy peaks at $\sim 0.7 \times 10^{51}$ erg. For models `m0.75` and `m0.55`, BH formation occurs at 1.36 s and 1.45 s, respectively, with similar peak energies around 2×10^{51} erg. The final explosion energies for models `m0.95`, `m0.75`, and `m0.55` are $\sim 0.06 \times 10^{51}$ erg, $\sim 0.72 \times 10^{51}$ erg, and $\sim 0.67 \times 10^{51}$ erg, respectively. We conclude that the final explosion energy and dynamics post-BH formation are primarily determined by the time interval between shock revival and BH formation. Contrary to what one would expect from 1D simulations (A. da Silva Schneider et al. 2020), we find that the `m0.75` and `m0.55` models peak at similar explosion energies. The `m0.75` model, being more explosive than the `m0.55`, expels more matter during the shock revival phase, thereby accreting less and delaying BH formation. Consequently, these two simulations are qualitatively and quantitatively similar. We interpret this similarity with caution since SNe are stochastic due to the turbulent nature of the explosion, exacerbated by the 2D hydrodynamics.

For each simulation, the binding energy outside the shock at BH formation exceeds the diagnostic explosion energy by more than an order of magnitude. Therefore, the phase between BH formation and $\sim$100 s, before the shock has entered the loosely bound envelope at every solid angle, is not trivial. We have paid particular attention to how the unbound region evolves during this critical phase. While $\sim 22\,M_\odot$ accretes during the first $\sim$100 s, the mass in the unbound region, located in the southern hemisphere, is $\lesssim 1.1\,M_\odot$ in each simulation. This multidimensional effect allows the high-energy unbound bubble to circumvent facing all of the overburden, such that the diagnostic explosion energy never drops to zero. In general, when the asymmetrical shock sequentially enters the low-density region as it passes the O–Ne/C interface between $\sim$10 and 100 s, the unbound region spreads to all solid angles, and the diagnostic explosion energy rises. After $\sim$100 s, matter is separated into ejecta and eventual accretion material, and a phase of slowly sweeping up the loosely bound outer $\sim 21.5\,M_\odot$ envelope follows.

The simulations presented here indicate that even if the diagnostic explosion energy drops to zero and no parcel is momentarily unbound, the loosely bound envelope can still be ejected if the shock survives. This is especially evident for the low-energy model, `m0.95`, which loses 99.4% of the diagnostic explosion energy after BH formation. Even so, the kinetic energy behind the shock drives up the diagnostic explosion energy again when unbinding the He/H envelope, resulting in a final ejecta mass of $\sim 21.7\,M_\odot$.

The unbound region for the two higher-energy models, `m0.75` and `m0.55`, undergo less relative mass and energy losses while passing through the oxygen core where the binding energy is high. The roughly 1.1 $M_\odot$ of material brought from low depths by the unbound bubbles carry the signatures of explosive nucleosynthesis, such as ^{56}Ni.

We have carefully tracked the composition of the unbound region and contextualized our understanding of the variable evolution curves of the different elements based on insights gained from the unbound region analysis. At BH formation there is a similar amount of ^{56}Ni in each model's unbound region, although the total ^{56}Ni produced increases with the effective mass. Effectively none of the heavy elements, from ^{44}Ti–^{60}Ni, including ^{56}Ni, remains unbound after $\sim$100 s for model `m0.95`. In contrast, models `m0.75` and `m0.55` eject $\sim$0.016 and 0.018 $M_\odot$ of ^{56}Ni, respectively. These two models, which bring roughly 1 $M_\odot$ more material from low radii, leave correspondingly less massive BHs behind.

The different explosion energies, ejecta masses, and compositions (particularly ^{56}Ni), will give rise to different electromagnetic transients. The duration and quality of the neutrino and gravitational-wave signals are also impacted by the thermal EOS. We postpone the study of multimessenger signals from BHSNe to future work.

If these events are realized in nature, the EOS affects the mass distribution of stellar-mass BHs through this formation channel. Beyond understanding the impact of the EOS on this formation channel, we encourage more studies on BHSNe in 2D and 3D to unveil its impact on the mass distributions of compact objects. This is an important and timely study, as these distributions are being revealed by data from both gravitational-wave interferometers (R. Abbott et al. 2023a) and X-ray observations (F. Özel & P. Freire 2016; J. M. Lattimer 2021). In the simulations presented here, the masses of the BH remnants are 24.02–25.48 $M_\odot$, rather than the progenitor mass at CC of $\sim$47.3 $M_\odot$, which is conventionally assumed in a failed SN scenario. Looking ahead, incorporating BHSNe into compact object population synthesis codes (e.g., S. Stevenson et al. 2017; N. Giacobbo & M. Mapelli 2018; K. Breivik et al. 2020) could prove fruitful.

Acknowledgments

We thank Matteo Bugli, Daniel Kresse, Finia Jost, Jesper Sollerman, Rodrigo Fernandez, Carl-Johan Haster, and Tuva Marken Ortman for their valuable discussions and insights throughout the course of this work. This work is supported by the Swedish Research Council (Project No. 2020-00452). The computations were enabled by resources provided by the National Academic Infrastructure for Supercomputing in Sweden (NAISS), partially funded by the Swedish Research Council through grant agreement no. 2022-06725. S.M.C. is supported by the U.S. Department of Energy, Office of Science, Office of Nuclear Physics, under award No. DE-SC0017955.

Software: FLASH (B. Fryxell et al. 2000), NuLib (E. O'Connor 2015), Matplotlib (J. D. Hunter 2007), NumPy (C. R. Harris et al. 2020), SciPy (P. Virtanen et al. 2020), yt (M. J. Turk et al. 2011), h5py (A. Collette 2013), and SkyNet (J. Lippuner & L. F. Roberts 2017).

Appendix
Nucleosynthesis for Select Positions

As described in Section 2.4, we perform our nucleosynthesis calculation on trajectories obtained from backward tracing in time starting for the moment of BH formation. In this appendix, for select positions at the time of BH formation, we show the thermodynamic properties along the trajectory as well as the evolution of the ^{4}He and ^{56}Ni abundances. The select trajectories highlight different regimes of nucleosynthesis and supports our discussion in Section 3.2 that for the most important unbound ejecta at the time of the BH formation the ^{56}Ni abundance has reached a steady state. In the left panel of Figure 17 we show a temperature slice at the time of BH formation for the `m0.55` simulation. The contours denote $T = 2$, 2.5, 3, 3.5, and 4 GK, which is also the range of the color scale. The shock front at this time coincides with the 2.5 GK contour. We label seven select positions, which we explore below. The arrow denotes the direction of the fluid velocity at the time of BH formation. There are several regions. Outside the shock the matter is cold at <2.5 GK. Position #4 is in this region. Within the shock, for $y > 0$, the fluid velocity is generally negative and matter, while shock heated, is slowly accreting and fueling the explosion in the south. Position #7 is in this region. In the interior of the southern region ($\sim -10^9$ cm $< y < 0$ and $x < \sim 0.4 \times 10^9$ cm), we have rapidly expanding winds from the PNS. This corresponds to the mass outflow (fueled by accretion elsewhere) that is continually driving the explosion until BH formation. Due to the rapid expansion, this material has low densities and temperatures. Position #6 is in this region. Surrounding this rapid expansion region, but still inside the shock, we have hotter, denser, and more slowly expanding unbound ejecta. Position #5 is in this region. Finally, the $\sim -1.5 \times 10^9$ cm $< y < 0$, $\sim 0.4 \times 10^9 < x < \sim 10^9$ cm region is a mixture of expanding shock heated material and ejecta from the PNS. Positions #1, #2, and #3 are in this region.

In the right panel of Figure 17, we show the temperature (top), the density (middle), and the ^{4}He (dashed) and ^{56}Ni (solid) mass fractions (bottom) for each of the positions denoted in the left panel and discussed above. We note that, for the composition panel, the scale transitions from linear to logarithmic at a mass fraction value of 0.1. The temperature and density of the trajectory before BH formation (denoted by the point at $\sim$1.45 s) is determined by our backward integration. The temperature and density of the trajectories following BH formation (for the purposes of this appendix) are set by the condition of adiabatic expansion (W. A. Fowler 1964; J. A. Harris et al. 2017):

$$T_i(t) = T_{i,\mathrm{BH}} \exp(-(t - t_{\mathrm{BH}})/3\tau^*), \quad \text{(A1)}$$

$$\rho_i(t) = \rho_{i,\mathrm{BH}} \exp(-(t - t_{\mathrm{BH}})/\tau^*), \quad \text{(A2)}$$

where $T_{i,\mathrm{BH}}$ and $\rho_{i,\mathrm{BH}}$ are, respectively, the temperature and density of the position i at the time of BH formation and τ^* is taken as 250 ms for simplicity. This certainly does not capture the hydrodynamic evolution after BH formation correctly, but rather approximately. The composition follows from SkyNet as discussed in Section 2.4. We note that for the main nucleosynthesis results presented in this paper we simply advect the composition determined from SkyNet at the time of BH formation, and therefore we do not utilize such an extrapolation within our simulations. As discussed below, this is reasonable for the unbound ejecta at the time of BH formation.

First we note that for all the trajectories from all the regions, there is little to no ^{56}Ni production after BH formation. The small exceptions are for positions #3 and #5. These are relatively (compared to position #6) slow trajectories of ejecta from the PNS. At the time of BH formation the temperatures are $\sim$3–3.5 GK and therefore some ^{56}Ni production, via ^{4}He capture on α-elements, occurs within the adiabatic expansion extrapolation regime in these tests. The remaining positions are too cold (or do not contain enough ^{4}He) at this time to effectively produce ^{56}Ni. Another interesting trajectory is position #1. This trajectory undergoes incomplete burning after reaching peak temperatures of only $\sim$4 GK at 0.8 s after bounce. The nucleosynthesis occurring at this point can be summarized as the remaining ^{16}O ($\sim$8%) being explosively burned into ^{40}Ca, ^{32}S, and ^{56}Ni. Ultimately, very little ^{56}Ni is produced (with a final mass fraction of $\sim$0.017). The majority of the mass at this position is silicon and sulfur (see Figure 2, at

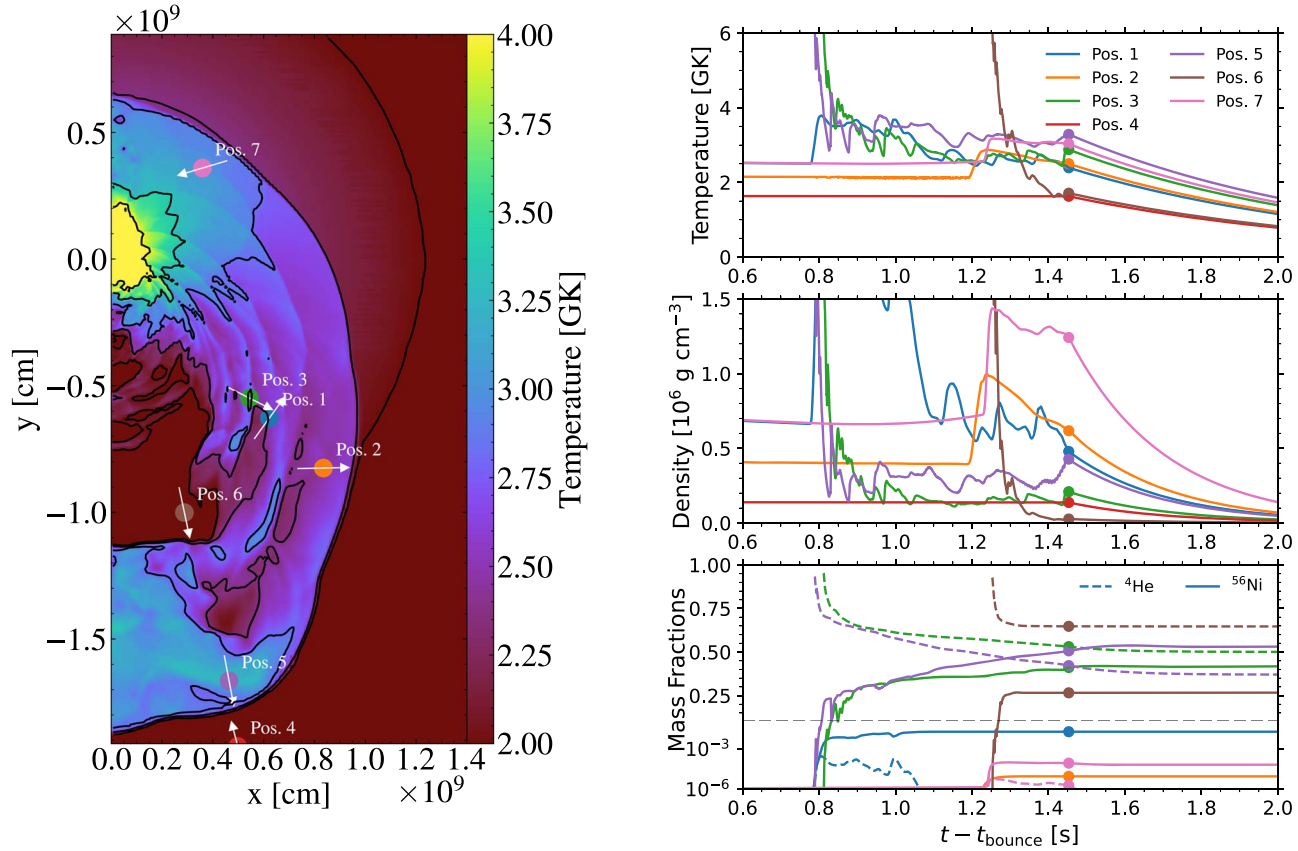


Figure 17. Left: temperature color map of the `m0.55` simulation at the time of BH formation. The contours mark $T = 2$, 2.5, 3, 3.5, and 4 GK, which is also the range of the color bar. Seven positions are marked with form the basis for the discussion in this appendix. Right: the temperature (top), density (middle), and ^{4}He (dashed) and ^{56}Ni (solid) mass fraction evolutions of each position marks in the left panel are shown. The dots denote the value at BH formation. The temperature and density following BH formation are set by adiabatic expansion (see text).

a radius of $\sim 8 \times 10^8$ cm, which is the starting radius of this particular trajectory), whose mass fractions change very little during the burning of the oxygen. We note that the trajectory does not include the energy generation from the burning itself.

ORCID iDs

Oliver Eggenberger Andersen https://orcid.org/0000-0002-9660-7952
Evan O'Connor https://orcid.org/0000-0002-8228-796X
Haakon Andresen https://orcid.org/0000-0002-4747-8453
André da Silva Schneider https://orcid.org/0000-0003-0849-7691
Sean M. Couch https://orcid.org/0000-0002-5080-5996

References

Abbott, R., Abbott, T. D., Acernese, F., et al. 2023a, PhRvX, 13, 011048
Abbott, R., Abbott, T. D., Acernese, F., et al. 2023b, PhRvX, 13, 041039
Adams, S. M., Kochanek, C. S., Gerke, J. R., & Stanek, K. Z. 2017, MNRAS, 469, 1445
Basinger, C. M., Kochanek, C. S., Adams, S. M., Dai, X., & Stanek, K. Z. 2021, MNRAS, 508, 1156
Baumgarte, T. W., Shapiro, S. L., & Teukolsky, S. A. 1996, ApJ, 458, 680
Belczynski, K., Doctor, Z., Zevin, M., et al. 2022, ApJ, 935, 126
Blondin, J. M., Mezzacappa, A., & DeMarino, C. 2003, ApJ, 584, 971
Boccioli, L., Gogilashvili, M., Murphy, J., & O'Connor, E. P. 2025, MNRAS, in press
Boccioli, L., Mathews, G. J., & O'Connor, E. P. 2021, ApJ, 912, 29
Boccioli, L., Roberti, L., Limongi, M., Mathews, G. J., & Chieffi, A. 2023, ApJ, 949, 17
Borges, R., Carmona, M., Costa, B., & Don, W. S. 2008, JCoPh, 227, 3191
Breivik, K., Coughlin, S., Zevin, M., et al. 2020, ApJ, 898, 71
Bruenn, S. W. 1985, ApJS, 58, 771
Buras, R., Janka, H.-T., Rampp, M., & Kifonidis, K. 2006, A&A, 457, 281
Burrows, A., Radice, D., Vartanyan, D., et al. 2019, MNRAS, 491, 2715
Burrows, A., & Vartanyan, D. 2021, Natur, 589, 29
Burrows, A., Vartanyan, D., & Wang, T. 2023, ApJ, 957, 68
Byrne, R. A., & Fraser, M. 2022, MNRAS, 514, 1188
Cardall, C. Y., & Budiardja, R. D. 2015, ApJL, 813, L6
Chan, C., Müller, B., & Heger, A. 2020, MNRAS, 495, 3751
Chan, C., Müller, B., Heger, A., Pakmor, R., & Springel, V. 2018, ApJL, 852, L19
Chevalier, R. A. 1989, ApJ, 346, 847
Colgate, S. A. 1971, ApJ, 163, 221
Collette, A. 2013, Python and HDF5 (Sebastopol, CA: O'Reilly)
Constantinou, C., Muccioli, B., Prakash, M., & Lattimer, J. M. 2015, AnPhy, 363, 533
Couch, S. M. 2013, ApJ, 765, 29
Couch, S. M., Carlson, J., Pajkos, M., et al. 2021, ParC, 108, 102830
Couch, S. M., & O'Connor, E. P. 2014, ApJ, 785, 123
Couch, S. M., Warren, M. L., & O'Connor, E. P. 2020, ApJ, 890, 127
Curtis, S., Ebinger, K., Fröhlich, C., et al. 2019, ApJ, 870, 2
da Silva Schneider, A., O'Connor, E., Granqvist, E., Betranhandy, A., & Couch, S. M. 2020, ApJ, 894, 4
da Silva Schneider, A., & OConnor, E. 2022, ApJ, 942, 16
da Silva Schneider, A. S., Roberts, L. F., Ott, C. D., & O'Connor, E. 2019, PhRvC, 100, 055802
De, K., MacLeod, M., Jencson, J. E., et al. 2024, arXiv: 2410.14778
Dubey, A., Reid, L. B., Weide, K., et al. 2009, ParC, 35, 512
Ebinger, K., Curtis, S., Ghosh, S., et al. 2020, ApJ, 888, 91
Eggenberger Andersen, O., Zha, S., da Silva Schneider, A., et al. 2021, ApJ, 923, 201
Einfeldt, B. 1988, in Proc. 16th Int. Symp., Shock Tubes and Waves (Weinheim: VCH), 671
Ertl, T., Janka, H.-T., Woosley, S. E., Sukhbold, T., & Ugliano, M. 2016, ApJ, 818, 124

Ertl, T., Woosley, S. E., Sukhbold, T., & Janka, H. T. 2020, ApJ, 890, 51
Fernández, R., Quataert, E., Kashiyama, K., & Coughlin, E. R. 2018, MNRAS, 476, 2366
Fowler, W. A. 1964, RvMP, 36, 545
Fröhlich, C., Hauser, P., Liebendörfer, M., et al. 2006, ApJ, 637, 415
Fryer, C. L. 1999, ApJ, 522, 413
Fryxell, B., Olson, K., Ricker, P., et al. 2000, ApJS, 131, 273
Giacobbo, N., & Mapelli, M. 2018, MNRAS, 480, 2011
Gogilashvili, M., Murphy, J. W., & Miller, J. M. 2024, ApJ, 962, 110
Harris, C. R., Millman, K. J., van der Walt, S. J., et al. 2020, Natur, 585, 357
Harris, J. A., Hix, W. R., Chertkow, M. A., et al. 2017, ApJ, 843, 2
Harten, A. 1983, JCoPh, 49, 357
Horowitz, C. J., Caballero, O. L., Lin, Z., O'Connor, E., & Schwenk, A. 2017, PhRvC, 95, 025801
Hunter, J. D. 2007, CSE, 9, 90
Ivanov, M., & Fernández, R. 2021, ApJ, 911, 6
Janka, H.-T., Melson, T., & Summa, A. 2016, ARNPS, 66, 341
Kifonidis, K., Plewa, T., Janka, H.-T., & Müller, E. 2003, A&A, 408, 621
Kochanek, C. S., Beacom, J. F., Kistler, M. D., et al. 2008, ApJ, 684, 1336
Kuroda, T., Kotake, K., Takiwaki, T., & Thielemann, F.-K. 2018, MNRAS, 477, L80
Lattimer, J. M. 2021, ARNPS, 71, 433
Lippuner, J., & Roberts, L. F. 2017, ApJS, 233, 18
Lovegrove, E., & Woosley, S. E. 2013, ApJ, 769, 109
Mapelli, M. 2021, in Handbook of Gravitational Wave Astronomy, ed. C. Bambi, S. Katsanevas, & K. D. Kokkotas, Vol. 16 (Berlin: Springer), 16
Marek, A., Dimmelmeier, H., Janka, H.-T., Müller, E., & Buras, R. 2006, A&A, 445, 273
Müller, B. 2015, MNRAS, 453, 287
Müller, B. 2020, LRCA, 6, 3
Müller, B., Heger, A., Liptai, D., & Cameron, J. B. 2016, MNRAS, 460, 742
Müller, B., Janka, H.-T., & Marek, A. 2012, ApJ, 756, 84
Müller, B., Melson, T., Heger, A., & Janka, H.-T. 2017, MNRAS, 472, 491
Nadezhin, D. K. 1980, Ap&SS, 69, 115
Nakamura, K., Takiwaki, T., Kuroda, T., & Kotake, K. 2015, PASJ, 67, 107
Neustadt, J. M. M., Kochanek, C. S., Stanek, K. Z., et al. 2021, MNRAS, 508, 516
O'Connor, E. 2015, ApJS, 219, 24
O'Connor, E., & Ott, C. D. 2011a, ApJ, 730, 70
O'Connor, E., & Ott, C. D. 2011b, arXiv: 1103.2117
O'Connor, E. P., & Couch, S. M. 2018a, ApJ, 854, 63
O'Connor, E. P., & Couch, S. M. 2018b, ApJ, 865, 81
Özel, F., & Freire, P. 2016, ARA&A, 54, 401
Pan, K.-C., Liebendörfer, M., Couch, S. M., & Thielemann, F.-K. 2018, ApJ, 857, 13
Pan, K.-C., Liebendörfer, M., Couch, S. M., & Thielemann, F.-K. 2021, ApJ, 914, 140
Pejcha, O., & Thompson, T. A. 2015, ApJ, 801, 90
Perego, A., Hempel, M., Fröhlich, C., et al. 2015, ApJ, 806, 275
Piro, A. L. 2013, ApJL, 768, L14
Powell, J., Müller, B., & Heger, A. 2021, MNRAS, 503, 2108
Quataert, E., Lecoanet, D., & Coughlin, E. R. 2019, MNRAS, 485, L83
Rahman, N., Janka, H. T., Stockinger, G., & Woosley, S. E. 2022, MNRAS, 512, 4503
Reynolds, T. M., Fraser, M., & Gilmore, G. 2015, MNRAS, 453, 2885
Sandoval, M. A., Hix, W. R., Messer, O. E. B., Lentz, E. J., & Harris, J. A. 2021, ApJ, 921, 113
Sedov, L. I. 1959, Similarity and Dimensional Methods in Mechanics (New York: Academic)
Shao, Y. 2022, RAA, 22, 122002
Shibata, M., Kiuchi, K., Sekiguchi, Y., & Suwa, Y. 2011, PThPh, 125, 1255
Sieverding, A., Waldrop, P. G., Harris, J. A., et al. 2023, ApJ, 950, 34
Skyrme, T. H. R. 1962, NucPh, 31, 556
Stevenson, S., Vigna-Gómez, A., Mandel, I., et al. 2017, NatCo, 8, 14906
Stockinger, G., Janka, H. T., Kresse, D., et al. 2020, MNRAS, 496, 2039
Sukhbold, T., Ertl, T., Woosley, S. E., Brown, J. M., & Janka, H.-T. 2016, ApJ, 821, 38
Sukhbold, T., Woosley, S. E., & Heger, A. 2018, ApJ, 860, 93
Sykes, B., Mueller, B., Cordero-Carrión, I., Cerdá-Durán, P., & Novak, J. 2023, PhRvD, 107, 103010
Sykes, B., & Müller, B. 2024, arXiv: 2410.04944
Timmes, F. X., & Swesty, F. D. 2000, ApJS, 126, 501
Toro, E. F., Spruce, M., & Speares, W. 1994, ShWav, 4, 25
Turk, M. J., Smith, B. D., Oishi, J. S., et al. 2011, ApJS, 192, 9
Ugliano, M., Janka, H.-T., Marek, A., & Arcones, A. 2012, ApJ, 757, 69
Virtanen, P., Gommers, R., Oliphant, T. E., et al. 2020, NatMe, 17, 261
Walk, L., Tamborra, I., Janka, H.-T., Summa, A., & Kresse, D. 2020, PhRvD, 101, 123013
Weaver, T. A., Zimmerman, G. B., & Woosley, S. E. 1978, ApJ, 225, 1021
Witt, M., Psaltis, A., Yasin, H., et al. 2021, ApJ, 921, 19
Wong, T.-W., Fryer, C. L., Ellinger, C. I., Rockefeller, G., & Kalogera, V. 2014, arXiv: 1401.3032
Yasin, H., Schäfer, S., Arcones, A., & Schwenk, A. 2020, PhRvL, 124, 092701
Zhang, W., Woosley, S. E., & Heger, A. 2008, ApJ, 679, 639